

Cite this: DOI: 00.0000/xxxxxxxxxx

A data-driven interpretation of the stability of molecular crystals

Rose K. Cersonsky,^{*a} Maria Pakhnova,^a Edgar A. Engel,^b and Michele Ceriotti^a

Received Date

Accepted Date

DOI: 00.0000/xxxxxxxxxx

Due to the subtle balance of intermolecular interactions that govern structure-property relations, predicting the stability of crystal structures formed from molecular building blocks is a highly non-trivial scientific problem. A particularly active and fruitful approach involves classifying the different combinations of interacting chemical moieties, as understanding the relative energetics of different interactions enables the design of molecular crystals and fine-tuning their stabilities. While this is usually performed based on the empirical observation of the most commonly encountered motifs in known crystal structures, we propose to apply a combination of supervised and unsupervised machine-learning techniques to automate the construction of an extensive library of molecular building blocks. We introduce a structural descriptor tailored to the prediction of the binding energy for a curated dataset of organic crystals and exploit its atom-centered nature to obtain a data-driven assessment of the contribution of different chemical groups to the lattice energy of the crystal. We then interpret this library using a low-dimensional representation of the structure-energy landscape and discuss selected examples of the insights that can be extracted from this analysis, providing a complete database to guide the design of molecular materials.

1 Introduction

Understanding molecular crystallization is critical to many fields of chemical sciences – from anticipating pharmaceutical stability and solubility^{1–5} to preventing⁶ or fostering⁷ aggregation in organic electronics to understanding complex formation in biological macromolecules^{8,9}.

Yet, molecular crystallization is a complex process that involves multiple cooperative and competing forces. Initial nucleation is typically motivated by strong interactions between functional groups^{10,11}. The structural patterns associated with these guiding interactions (deemed “supramolecular synthons”) and their hierarchies are often the focus of experimental and computational studies in crystal structure prediction^{12,13}. Nevertheless, once molecules have moved within closer range, many factors, including weaker interactions, the expulsion of solvent molecules, and geometric packing, will then determine the short- and potentially long-range order, leading to many potentially-stable polymorphs for a given stoichiometry. In the past decades, there has been a growing push to develop a “holistic” view of molecular crystallization^{14,15}, not only taking into account the nearest-neighbor contacts but also the interplay of these interactions with other components of the molecular assembly.

Thus, molecular crystallization has emerged as a hotbed for computational inquiry, as the interplay of many competing interactions necessitates diverse, high-throughput studies¹⁴. This focus has led to considerable theoretical and software developments for qualitative and quantitative analyses, including those tailored to crystal structure prediction (CSP)^{16–19} and the representation of electrostatic surfaces and molecular geometry^{20,21}. Even more recently, machine learning has been used to understand the individual configurational and energy landscapes of molecules^{22–28}; however, such techniques have yet to be applied in the general, holistic vein required to extract the qualitative insights that can be used to support crystal design efforts.

To study molecular crystallization in this broad lens, we have curated a dataset of nearly 3'400 C+H+N+O+S-containing molecular crystals from those reported in Cordova *et al.*²⁹ to capture a wide range of molecular interactions. We computed the binding energy for each of these crystals using DFT calculations of each crystal and its relaxed molecular components. We build a regression model for this lattice energy, demonstrating the improvements in accuracy and reduction in model complexity from using a physics-informed approach. We then demonstrate how a combination of supervised and unsupervised machine learning models can determine and assist in interpreting molecular moieties' intermolecular interactions. We have made our datasets, and analyses openly-available through the Materials Cloud³⁰, with interactive components aimed to guide future molecular design and narrower or targeted studies.

^a Laboratory of Computational Science and Modeling (COSMO), École Polytechnique Fédérale de Lausanne, Lausanne, Switzerland

^b TCM Group, Trinity College, Cambridge University, Cambridge, UK

* Present address: Rose.Cersonsky@epfl.ch

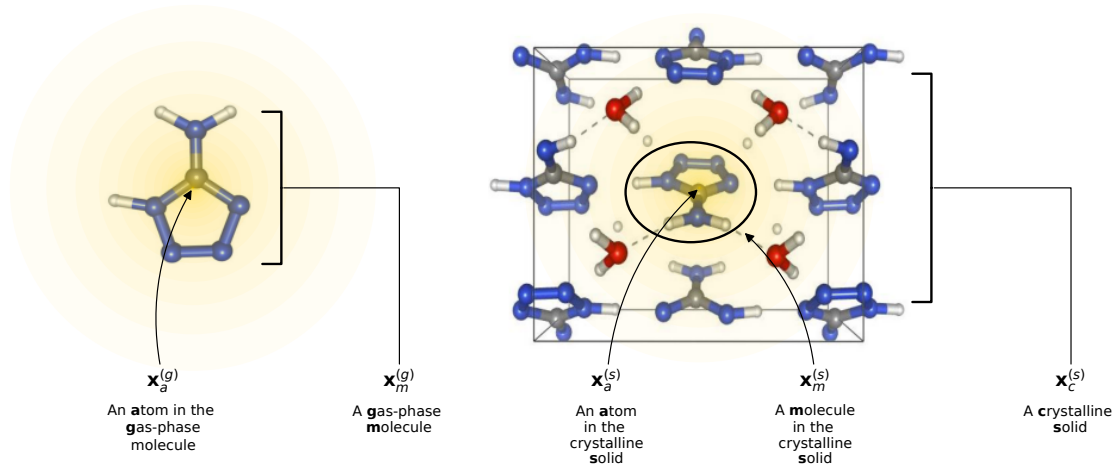


Fig. 1 Visualization of Descriptor Notation, as described in Sec. 2.1, visualized for 5-Aminotetrazole Monohydrate (CSD Ref. AMTETZ³¹). Each descriptor contains the information of an atom and its neighborhood (shown in yellow shading).

2 Notation

In this study, we employ atom-centered descriptors³² to identify the contributions of specific collections of atoms to the binding of a crystal. Given the many atomic and energetic entities (atoms, molecules, crystals, total energy versus lattice energy), we will rely on many numerical representations and equations; hence we start by establishing a consistent notation we will use throughout the text.

2.1 Descriptors

To reflect the physics of atomic interactions, we use symmetry-adapted descriptors to encode/describe the geometric arrangement of atoms in their atomistic configurations, specifically the 3-body SOAP descriptors outlined in Appendix B.1. Each of these input descriptors is written as $\mathbf{x}_\sigma^{(i)}$, where the subscript σ signifies the collection of atoms being described, including the entire crystal (c), a molecule (m), or an atom (a). n_σ is the number of atoms in the given collection. Because we discuss analogous atoms or molecules in both the solid and gas phases, we use the superscript (i) to denote the phase (crystalline solid (s) or dilute gas (g)).

The descriptor for a given collection should be assumed as the average of the descriptors for the constituent atoms:

$$\mathbf{x}_\sigma^{(i)} = \frac{1}{n_\sigma} \sum_{a \in \sigma} \mathbf{x}_a^{(i)}. \quad (1)$$

For example, the descriptor for the atoms in a molecule in a dilute gas is $\mathbf{x}_m^{(g)} = \frac{1}{n_m} \sum_{a \in m} \mathbf{x}_a^{(g)}$. If we were to look at the same molecule in the crystalline solid we would get $\mathbf{x}_m^{(s)} = \frac{1}{n_m} \sum_{a \in m} \mathbf{x}_a^{(s)}$. A schematic of these concepts is shown in Fig. 1, using the co-crystal 5-Aminotetrazole Monohydrate (CSD Ref. AMTETZ³¹) as an example.

2.2 Energies and Regressions

We use \mathbf{E}_σ to denote the total energy of a collection of atoms and $\mathbf{e}_\sigma \equiv \mathbf{E}_\sigma/n_\sigma$ to indicate the per-atom energy. Constructing linear models for the atomic energies amounts to the ansatz

$$\mathbf{e}_\sigma = \mathbf{x}_\sigma \mathbf{w}_\sigma + \epsilon_\sigma \quad (2)$$

where \mathbf{w}_σ is the regression weights and ϵ_σ the residual errors. The *lattice energy* (also referred to as the *binding* or *cohesive* energy in literature) of a molecular crystal is given by Δ_c , where

$$\Delta_c = \mathbf{E}_c - \sum_{m \in c} \mathbf{E}_m. \quad (3)$$

With the average lattice energy per atom given by

$$\delta_c \equiv \Delta_c/n_c = \mathbf{e}_c - \sum_{m \in c} \frac{n_m}{n_c} \mathbf{e}_m \quad (4)$$

Later, we will use our regression model to determine the atomic contributions to the lattice energy, which we will denote δ_a , where $\delta_c = \frac{1}{n_c} \sum_{a \in c} \delta_a$. We will also consider the contributions for different collection of atoms, and will denote the average lattice energy contribution as $\delta_\sigma = \frac{1}{n_\sigma} \sum_{a \in \sigma} \delta_a$. When we regularize these contributions using a Gaussian filter (discussed in Sec. 3.2 and Appendix B.2), we will use a tilde to give $\tilde{\delta}$.

3 Results and Discussion

In the following, we consider crystals and gas-phase molecules, both of which have been geometry-optimized by minimizing their configurational energies with respect to the atomic positions, as described in Appendix A. Unless stated otherwise, we use as our featurization the 3-body SOAP vectors (as described in Appendix B.1 and computed with `librascal`³³) and build 5-fold cross-validated ridge regression models using `scikit-learn`³⁴. All models were trained on the same training set of 2'823 crystals (or the corresponding 3'242 molecules). We report errors on a mutually-exclusive set of 558 crystals (or the corresponding 628 molecules).

Regression Equation	Eq.	RMSE	MAE
$\mathbf{e}_c = \mathbf{x}_c^{(s)} \mathbf{w}_c$	(2)	1.096	0.838
$\mathbf{e}_m = \mathbf{x}_m^{(g)} \mathbf{w}_m$	(2)	0.613	0.465
$\delta_c = \mathbf{x}_c^{(s)} \mathbf{w}_c - \sum_{m \in c} \frac{n_m}{n_c} (\mathbf{x}_m^{(g)} \mathbf{w}_m)$	(5)	0.949	0.707
$\delta_c = \mathbf{x}_c^{(s)} \mathbf{w}$		0.774	0.556
$\delta_c = \mathbf{x}_c^{(g)} \mathbf{w}$		1.07	0.723
$\delta_c = \mathbf{x}_c^{(s-g)} \mathbf{w}$	(7)	0.605	0.445
$\delta_c = \{\mathbf{x}_c^{(s)}, \mathbf{x}_c^{(g)}\} \mathbf{w}$		0.615	0.436

Table 1 Results of Linear Regression Exercises. In each linear regression, an independent, 5-fold cross-validated model was built on 2'823 crystals (or the 3'242 coinciding molecules). Here we report the errors (in kJ/mol) on a separate set of 558 crystals (or the coinciding 628 molecules). In each regression equation \mathbf{w} is unique to that regression.

3.1 Building a Model for the Lattice Energy

One can estimate the atomic contributions to a target property (and thereby assess the contributions of specific molecular motifs) by building a robust machine learning model on an atom-centered descriptor³⁵. Suppose we have a descriptor

$$\mathbf{x}_\sigma = \frac{1}{n_\sigma} \sum_{a \in \sigma} \mathbf{x}_a$$

and train a regression model on some target y such that $y = \mathbf{x}_\sigma \mathbf{w} + \epsilon$, where \mathbf{w} is the regression weight and ϵ is the residual error from the regression. We can then estimate the approximate contribution of each atom by computing $y_a = \mathbf{x}_a \mathbf{w}$.

Given Eq. (4), it is possible to build a model for the lattice energy from two separate models for crystal and molecular energy

$$\delta = \mathbf{x}_c^{(s)} \mathbf{w}_c + \epsilon_c - \sum_{m \in c} \frac{n_m}{n_c} (\mathbf{x}_m^{(g)} \mathbf{w}_m + \epsilon_m). \quad (5)$$

Eq. (5) may then be rewritten as:

$$\delta = \mathbf{x}_c^{(s)} \mathbf{w}_c - \mathbf{x}_c^{(g)} \mathbf{w}_m + \epsilon \quad (6)$$

where we have defined $\epsilon \equiv \epsilon_c - \sum_{m \in c} \frac{n_m}{n_c} \epsilon_m$. In this scheme, the regression of the lattice energy is implicitly limited by the errors of the independent regressions; therefore, given a good fit for \mathbf{e}_c and \mathbf{e}_m , this is a fairly robust way to predict the lattice energy.

When we predict the crystal and molecular atomic energies \mathbf{e}_c and \mathbf{e}_m , we obtain RMSEs of 1.096 kJ/mol and 0.613 kJ/mol, respectively, which are acceptably small compared to the intrinsic variance of the baselined* target energies of the test set, which have standard deviations of 4.547 kJ/mol and 4.252 kJ/mol, respectively. However, the intrinsic variance of the lattice energies is smaller (2.095 kJ/mol); therefore, the resulting RMSE of 0.949 kJ/mol from Eq. (5) is very unsatisfactory and suggests that

the errors in the independent regressions generally overlap with the lattice energy contributions.

With the reduced variance of the target (lattice energy), it thus makes sense to construct the regression model directly on our target. Building a regression on $\mathbf{x}_c^{(g)}$, while conceptually nonsensical (the descriptors of the molecules contain no information on the intermolecular interactions), yields an RMSE of 1.07 kJ/mol. The similarity of this result to that obtained by Eq. (6) underscores the poor performance of combining the separate, independent regressions. Regressing on $\mathbf{x}_c^{(s)}$ improves the regression substantially, achieving an RMSE of 0.774 kJ/mol.

Yet, conceptually, neither of these two representations ($\mathbf{x}_c^{(s)}$ and $\mathbf{x}_c^{(g)}$) contain the full set of relevant information – the molecular descriptor $\mathbf{x}_c^{(g)}$ is missing information on intermolecular interactions, and the crystal descriptor $\mathbf{x}_c^{(s)}$ is unaware of the conformational changes that the molecules undergo upon crystallization. The necessity of this missing information is confirmed when we regress on concatenated descriptors $\{\mathbf{x}_c^{(s)}, \mathbf{x}_c^{(g)}\}$ and our RMSE drops to 0.615 kJ/mol.

Furthermore, Eq. (6) provides another way to similarly (and more explicitly) encode the nature of the problem into our choice of representation. Given a descriptor that appropriately distinguishes between periodic crystals and molecules, a regression model can predict their energies using the same regression weights, $\mathbf{w} = \mathbf{w}_c = \mathbf{w}_m$. Substituting this into Eq. (6),

$$\delta = \mathbf{x}_c^{(s)} \mathbf{w} - \mathbf{x}_c^{(g)} \mathbf{w} + \epsilon = \mathbf{x}_c^{(s-g)} \mathbf{w} + \epsilon \quad (7)$$

where we define $\mathbf{x}_c^{(s-g)} \equiv (\mathbf{x}_c^{(s)} - \mathbf{x}_c^{(g)})$ as the so-called ‘‘remnant’’ descriptor and ϵ again denotes the residual errors. Explicitly adapting our representation $\mathbf{x}_c^{(s-g)}$ to the nature of the lattice energy results in a similar result to learning on $\{\mathbf{x}_c^{(s)}, \mathbf{x}_c^{(g)}\}$: 0.605 kJ/mol, despite being in a smaller feature space. Conceptually, this descriptor still encodes the 3-body correlation between an environment and its neighbors but explicitly incorporates the change in molecular geometry upon crystallization and reduces the weights of atomic triplets whose interactions are primarily intramolecular and/or the same in gas and solid phase.

This result is mirrored in non-linear regression models, where again, a superior result is obtained by either constructing a kernel on $\mathbf{x}_c^{(s-g)}$ or taking the difference of non-linear feature vectors (see Appendix C.2). An optimized RBF kernel on the remnant descriptors yields a similar RMSE to the linear model. We get some improvement (by ~ 0.06 kJ/mol compared to the best linear model) by taking the difference of the implicit RKHS features defined by the kernels of the crystalline and molecular descriptors. This result further emphasizes the rationale behind the remnant approach, and suggests that one can improve accuracy by combining non-linear feature constructions to mimic the mathematical formulation of target properties. Similar conclusions were obtained using a parameter-free kernel, also in Appendix C.2.

When the molecular geometry is known *a priori*, these results suggest that linear and non-linear regressions for the lattice energy should be built on descriptors conceptually akin to $\mathbf{x}_c^{(s-g)}$, rather than $\mathbf{x}_c^{(s)}$, as has been common practice in the literature^{23,25,27,28}.

* To improve the regressions of crystal and molecular energies, we subtract a *baseline* determined by linear regression of the atomic composition on the total energies.

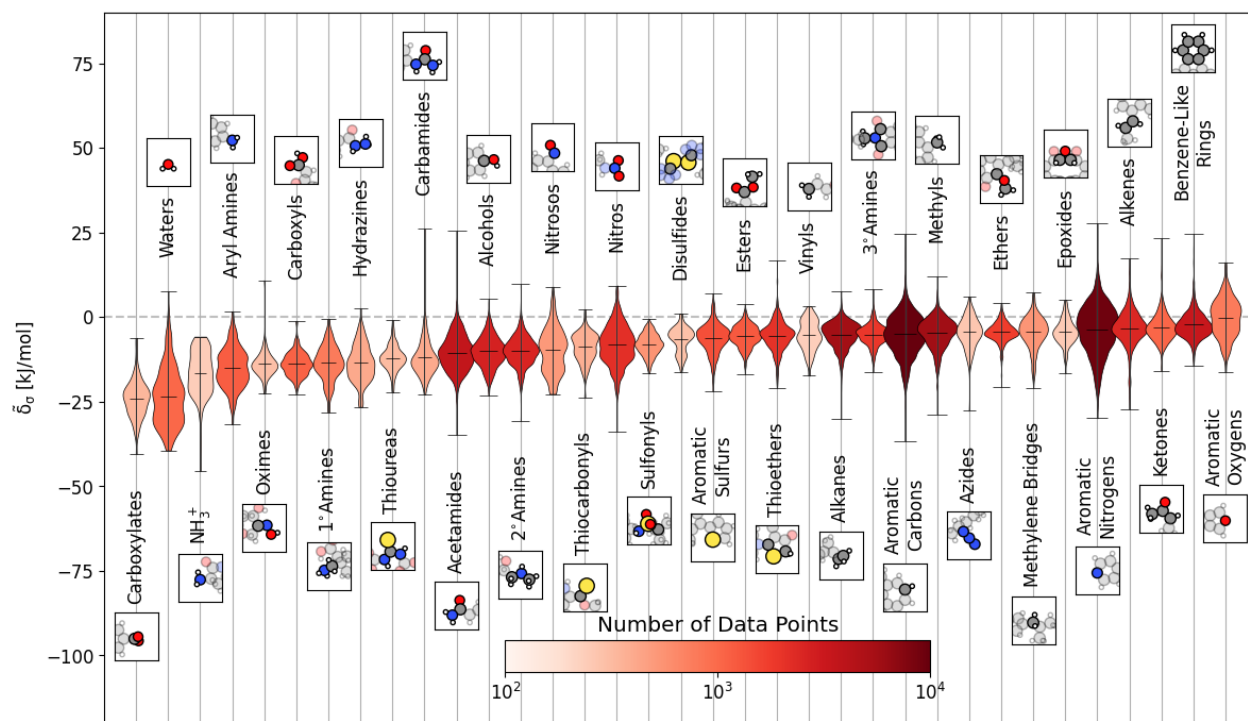


Fig. 2 Distribution of Energetic Contributions for Different Functional Groups. For each functional group, a representative example is shown above or below the violin plot with the functional group highlighted. We have limited this figure to those functional groups with more than 200 instances in the dataset (see Fig. S3 for all groups). The lines on each plot denote each group’s extreme and mean contributions. The plots are colored by the number of examples within the dataset, ranging from 7 (Sulfonamide, not shown) to 12’161 (Aromatic Carbon).

3.2 Identifying High-Stability Motifs

With our target-adapted regression model, we can assign effective contributions to each atomic environment, where we take the remnant descriptor of each atomic environment and compute

$$\delta_a = \mathbf{x}_a^{(s-g)} \mathbf{w}. \quad (8)$$

Despite the mathematical logic behind this step, the lack of physical underpinnings for this decomposition may result in energy being arbitrarily partitioned between neighboring atoms. This leads to disproportionately large contributions of opposite size being assigned to each atom, not dissimilar to how a regression model may be overfit by assigning large regression weights. To ease this effect, we can apply a Gaussian filter to each δ_a . For the i^{th} atom, this results in

$$\tilde{\delta}_i = \sum_j \delta_j \frac{f(i,j)}{\sum_k f(j,k)} \quad (9)$$

where \sum_j runs over all neighbors of i and \sum_k runs over all neighbors of j (defined by a cutoff of 2\AA). For neighbors a and b and interatomic distance d_{ab} , $f(a,b) = \exp[-d_{ab}^2/2\zeta^2]$. This procedure, introduced for the electronic density of states in Ben Mahmoud *et al.*³⁶, has the effect of regularizing the decomposition while maintaining the regression results, *i.e.*, $\delta = \frac{1}{n_c} \sum_{a \in c} \delta_a = \frac{1}{n_c} \sum_{a \in c} \tilde{\delta}_a$. We show the effect of this filter on the distribution of atomic contributions in Appendix B.2. It is worth to compare our data-driven decomposition with one based on an empirical model of interactions, or with one of the many atoms-in-molecules de-

compositions of the energy computed by quantum-chemical calculations. On one hand, our approach makes it harder to explicitly interpret the stabilizing power of a motif in terms of physical terms (electrostatics, dispersion....). On the other, in many cases forcefields and energy decompositions have a high degree of arbitrariness, and the accurate prediction of the total cohesive energy comes from a cancellation of errors in the individual components. The atomic contributions Eq. (9) are obtained with the only requirement of being smooth, and (since they are built using a remnant descriptor) to correlate with the structural features that are associated with the crystal-forming process. As we shall see, their nature allows one to recognize the role played by collective effects - such as steric hindrance, or molecular distortions - contributing to the holistic view of lattice stability that is one of the goals of this study.

Taking the 3’242 molecules from our training set, we use SMARTS descriptors³⁷ and RDKit Substructure Matching³⁸ to identify the atoms belonging to common molecular motifs, finding approximately 70’000 motifs. Details of this procedure and our table of SMARTS strings are given in Appendix B.3 and Table S1, respectively. For each motif, we determine the effective cohesive interaction $\tilde{\delta}_\sigma$ as the average of all atomic contributions found using Eq. (8) and Eq. (9).[†]

[†] The lattice energy of the crystal is not the sum of these motif contributions, as 1) both are averaged quantities, and 2) a single crystal may have multiple overlapping motifs.

We plot the span of lattice energy contributions for motifs with greater than 200 instances in the dataset in Fig. 2[‡]. The functional groups are arranged in order of increasing average cohesive interactions, from carboxylates and quaternary ammonium groups (both found in several zwitterionic molecules) to oxygen atoms found in aromatic rings. We see a clear trend in the nature of the functional groups from left to right. On the left (the motifs leading to the strongest intermolecular interactions), there are groups typically associated with hydrogen bonding (e.g., carboxyls and waters) and charged groups found in zwitterionic molecules (e.g., NH_3^+ and carboxylates). As we move to the right, the molecular motifs are, on average, weakly binding, with the largest range of interactions coming from the most broadly-defined groups, including the alkanes, alkenes, and carbons or nitrogens in aromatic rings.

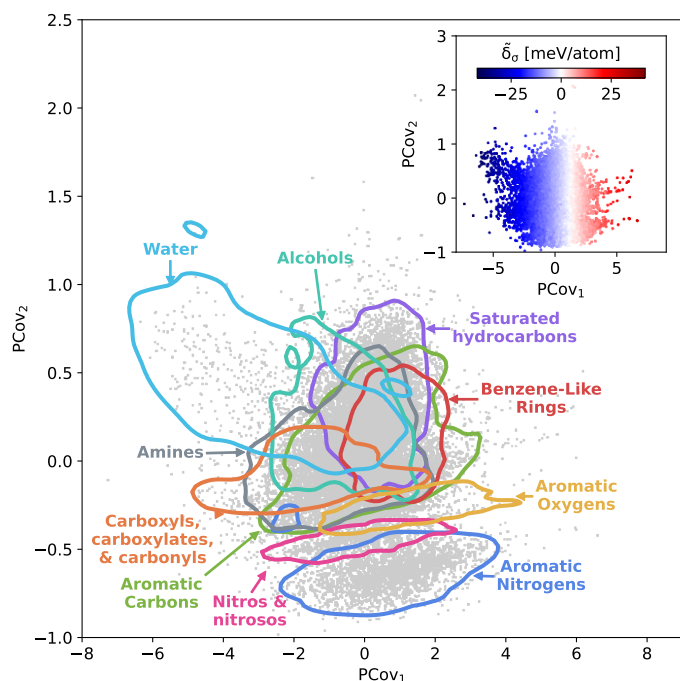


Fig. 3 Principal Covariates Regression (PCovR) Map of the Interactions of Molecular Motifs. A structure-property map of molecular motifs, denoting major classes of motifs and outlining the regions where the 95th percentile of these motifs occur. (inset) the same map colored by the cohesive interactions, ranging from blue (strongly attractive) to white (neutral) to red (strongly resistant).

This trend is further demonstrated by plotting the structure-property map of all motifs using *Principal Covariates Regression* (PCovR), a hybrid supervised-unsupervised dimensionality reduction technique first introduced in De Jong and Kiers³⁹ and adapted to chemical systems in Helfrecht *et al.*⁴⁰. This technique produces a latent-space mapping that arranges different motif classes based on their structural similarity and correlation to a set of target properties. In Fig. 3, we show a map using the average remnant descriptor for each motif and their average energy contribution, using contour lines to show where 95% of such motifs

fall on the PCovR map. One sees that, in this case, the first axis of this plot (PCov₁) correlates strongly with the (learnable) cohesive interactions. The second axis (PCov₂) allows us to resolve structural differences between motifs with similar energetic contributions. In this mapping, we can learn from the spread of each group. For example, the approximately 1'000 water molecules (light blue in Fig. 3) span the greater portion of the left-hand side of the figure, highlighting the chemical diversity of intermolecular water interactions. Juxtapose this with the approximately 2500 nitro and nitroso groups (pink in Fig. 3) that span a smaller region in PCovR space, implying a narrower range of intermolecular interactions. Here we have combined several groups for visual simplicity; however, we have included subplots highlighting each functional group in Figs. S5 - S8, including the sample sizes and range of contributions.

The PCovR framework presents a blueprint for analyzing the interactions of different structural motifs – given a single motif type, what characteristics of a molecular environment lead to a more stabilizing interaction? In the following sections, we will take a look at the stabilizing environments for a few classes of functional groups, starting with the well-known stabilizing interactions of water and carboxylic groups, then moving onto two groups with a wide range of intermolecular interactions, 6-membered aromatic carbon rings and nitro groups. With each functional group, we generate a new PCovR only using the averaged remnant descriptors and effective interactions for the instances of that group, such that the structural diversity embedded in the map reflects the diversity of *interactions*, rather than the diversity of the molecules themselves. We have included similar maps for all other molecular motifs in an online data repository⁴⁵ hosted by Materials Cloud³⁰.

3.2.1 Waters

We begin with a ubiquitous molecular crystal stabilizer: water. The estimated contributions of the 1'030 water molecules in this dataset span a range of -37.4kJ/mol to 5.2kJ/mol, with the majority of interaction strengths occurring at around -23.4 ± 7.8 kJ/mol. We generate a new PCovR shown in the left panel of Fig. 4. On the right side of Fig. 4, we have included a panel showing the crystalline conformation and molecules recolored by δ_a (using the same scale as in the left panel).

First, we look at a common parameter for measuring the stabilizing effect of water: hydrogen bonding (H-bonding). Here, we have calculated H-bonds based on when the $\text{O} \cdots \text{H}$ or $\text{H} \cdots \text{X}$ distance is less than 2.5 \AA and the dihedral angle of $\text{O} \cdots \text{H-X}$ or $\text{OH} \cdots \text{X}$ is greater than 150° . From the lower left of Fig. 4, we see that the number of H-bonds donated to the water molecule ($\text{O} \cdots \text{H}$) does not correlate with the cohesive interaction of the water molecules (Pearson correlation coefficient, or PCC, of -0.12). There is some qualitative correlation/anti-correlation between the nature of these donated H-bonds and the second principal covariate, yet still not particularly strong (PCC=0.37,-0.42 for the number of $\text{O} \cdots \text{H-N}$ and $\text{O} \cdots \text{H-O}$, respectively). There is a mild anti-correlation between the number of H-bonds the water itself donates ($\text{OH} \cdots \text{X}$), with a PCC of -0.31. However, the second principal covariate

[‡] We have included a similar figure with the full span of molecular motifs in Fig. S3

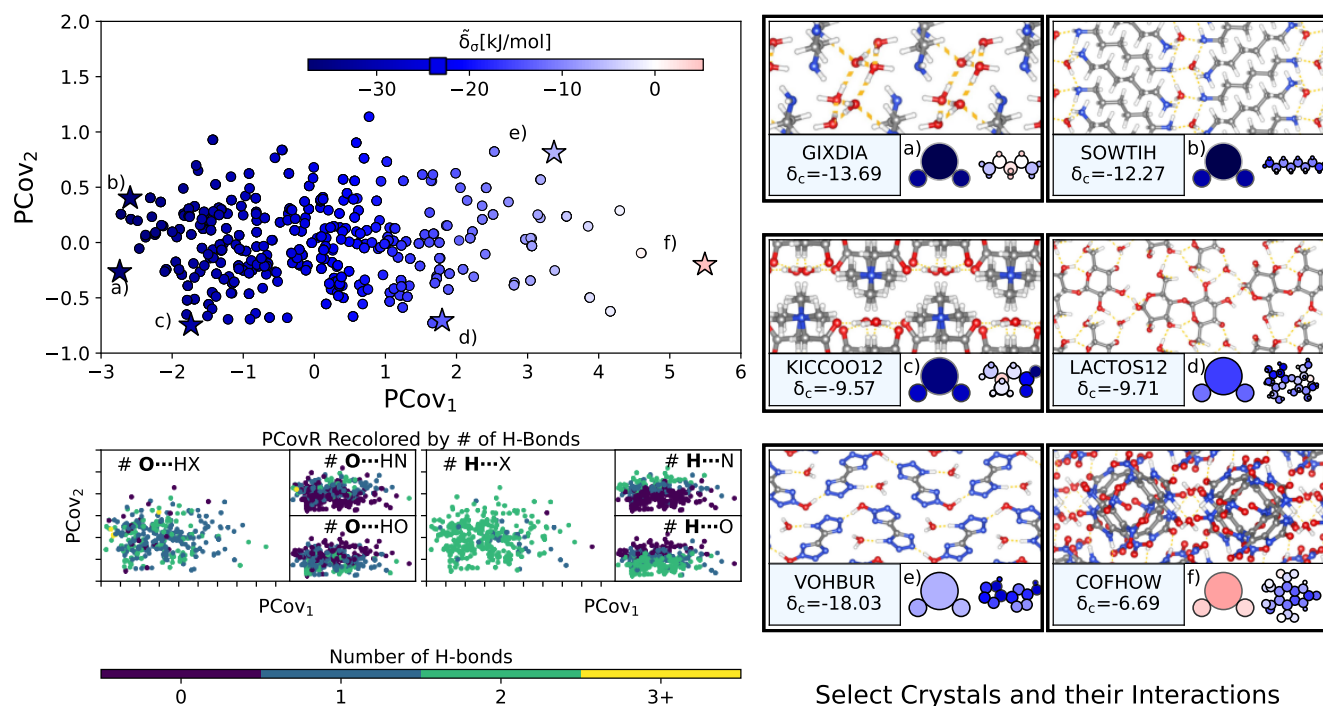


Fig. 4 The Interactions of Water Molecules. (left) Principal Covariates Regression (PCovR) map, where the color of each point denotes the estimated cohesive interaction of that motif and a marker on the color bar denotes the average value for all waters. Below the large PCovR map, we have shown the same map recolored by the number of hydrogen bonds (H-bonds), separating those donated to the oxygen atom (left) from those donated by the hydrogen atoms (right). The insets on the right visualize several extremal or interesting environments. (right) Select crystalline configurations and energy assignments: CSD Refs. (a)GIXDIA⁴¹, (b)SOWTIH⁴¹, (c) KICCOO12⁴², (d) LACTOS12⁴³, (e) VOHBUR⁴⁴, and (f) COFHOW. In each panel on the right, the bottom row shows the total lattice energy of the crystal (in kJ/mol) and the corresponding molecules where the atoms have been recolored by their estimated lattice energy contribution (on the same scale as on the left panel).

is strongly correlated and anti-correlated with the nature of these interactions, with the number of OH \cdots N and OH \cdots O interactions achieving a PCC of 0.69 and -0.71, respectively. Waters with primarily OH \cdots N-type hydrogen bonds are at the top of the map (e.g., Fig. 4(e), CSD Ref. VOHBUR⁴⁴), with OH \cdots O-type at the bottom of the map (e.g., 6-(hydroxymethyl)-5-((3,4,5-trihydroxy-6-(hydroxymethyl)tetrahydro-2H-pyran-2-yl)oxy)tetrahydro-2H-pyran-2,3,4-triol monohydrate, Fig. 4(d), CSD Ref. LACTOS12⁴³).

This analysis emphasizes that the number of hydrogen bonds does not fully capture all of the nuances of water stabilization – the majority of water molecules participate in 2-3 such interactions, and the energy of these bonds can span a wide range. In O \cdots H-X interactions, there is little energetic difference based on whether the acceptor is a nitrogen or oxygen atom – both types of hydrogen bonds span the full range of energies. The nature of the acceptor is encoded in the covariate orthogonal to the chemical features most correlated with interaction strength (*i.e.*, the nature of the acceptor is primarily correlated with the second covariate).

Unsurprisingly, we see that the strongest water interactions in 1,3-Diaminopropane trihydrate (CSD Ref. GIXDIA⁴¹, Fig. 4(a)) and 1,6-Diaminohexane monohydrate (CSD Ref. SOWTIH⁴¹, Fig. 4(b)), where the water molecules associate with other water molecules and the amine group of their co-crystalline molecule. Our weakest contribution, by far, occurs in 4,5,6,7-Tetranitro-1,3-dihydro-2H-benzimidazol-2-one

hemihydrate (CSD Ref. COFHOW, Fig. 4(f)), where the water molecules sit interstitial to the imidazole molecules, prohibited from forming hydrogen bonds and potentially interfering with the stabilization of the imidazole clusters.

3.2.2 Carboxylic Acid Groups

As a strong electron donor, carboxylic acids are considered a key motif in molecular crystallization^{21,51,52}, which is supported by their strong negative lattice energy contribution, here ranging from -23.4 kJ/mol to -0.9 kJ/mol, with the majority of interaction strengths occurring in the -13.7 ± 3.4 kJ/mol range. Taking the 1'109 carboxylic acid groups, we generate a new PCovR shown in the left panel of Fig. 5. On the right side of Fig. 5, we have included a panel showing, for select motifs, the crystalline conformation and molecules recolored by δ_a (using the same scale as in the left panel).

The strongest contributions are found in 1,2-Di(2-pyridyl)ethylene (CSD Ref. FIBHOP⁴⁶) in a succinic acid molecule (Fig. 5(a)) that forms two sets of supramolecular synthons: one homosynthon with the other succinic acid (Fig. 5(b)), and one heterosynthon with the pyridine group (consistent with the literature on the strength of carboxylic-pyridine interactions⁵³⁻⁵⁵). Interestingly, this crystal also contains one of the most weakly interacting groups (Fig. 5(b)), in the second succinic acid molecule that only participates in the single homosynthon.

Carboxylic acids form the strongest cohesive interactions when

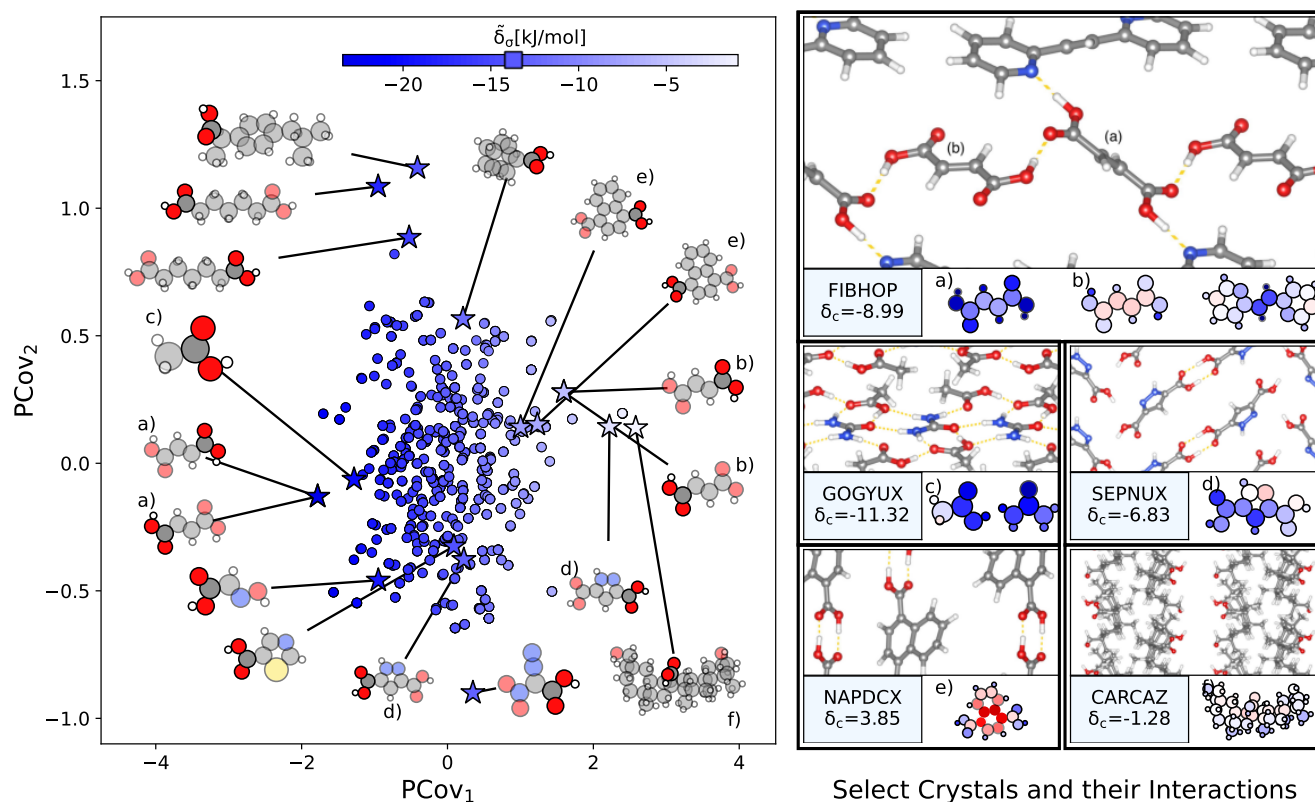


Fig. 5 The Interactions of Carboxylic Acid Groups. (left) Principal Covariates Regression (PCovR) Map, where the color of each point denotes the estimated cohesive interaction of that motif, and a marker on the color bar denotes the average value for all carboxylic acid groups. The insets visualize several extremal or interesting motifs. (right) Select crystalline configurations and energy assignments: CSD Refs. (a,b) FIBHOP⁴⁶, (c) GOGYUX⁴⁷, (d) SEPNUX⁴⁸, (e) NAPDCX⁴⁹, and (f) CARCAZ⁵⁰. In each panel on the right, the bottom row shows the total lattice energy of the crystal (in kJ/mol) and the corresponding molecules where the atoms have been recolored by their estimated lattice energy contribution.

participating in multiple synthons, particularly heterosynthons (and typified by Fig. 5(a) and (c), and noted in earlier literature⁵⁶). Moving to the right, we see the contribution decrease commensurate to the number of interactions. For example, in 3,5-Pyrazoledicarboxylic acid (CSD Ref. SEPNUX⁴⁸, Fig. 5(d)), there are two carboxylic acid groups that have drastically different energy contributions – one that forms a doublet homosynthon and the other is without direct interaction. In an extreme case (CSD Ref. CARCAZ⁵⁰, Fig. 5(f)), the carboxylic acid group is prevented from interacting due to the bulkiness of the overall molecule, leading to a neutral contribution.

An interesting success of this energy assignment is the ability to identify stabilizing motifs in otherwise unstable or metastable crystals. For this reference DFT method, 1,4-Naphthalenedicarboxylic acid (CSD Ref. NAPDCX⁴⁹, Fig. 5(e)) has an overall positive lattice energy, yet we can clearly identify a binding interaction between carboxylic acid groups.

3.2.3 6-Membered Unsaturated Carbon Rings

6-member unsaturated carbon rings (consistent with benzene molecules but more broadly-defined to include branched rings) show weak intermolecular interactions ranging from -13.3 kJ/mol to 23.2 kJ/mol, with the majority of interactions occurring in the -2.2 ± 3.8 kJ/mol range. Similar to Sec. 3.2.2, we generate a new PCovR using the averaged remnant descriptors and effec-

tive interactions using the 3'348 benzene-like motifs, as shown in the left panel of Fig. 6. Again, we have included a panel on the right showing the crystalline conformation and molecules colored by $\bar{\delta}_a$ for select configurations.

The most strongly-binding benzene-like motifs occur in molecules where 1) the ring is functionalized by strongly interacting groups, 2) the interactions of these groups facilitate planar molecular geometry, and 3) stacking occurs between the benzene-like rings with these auxiliary groups. Perhaps the best example of this is 2,4,6-trinitrobenzene-1,3,5-triamine (CSD Ref. TATNBZ03⁵⁷, Fig. 6(a)), where the aromatic carbon ring stacks above the primarily *intramolecular* nitro-amine interaction. This is also visible in Fig. 6(b), a derivative of CSD Ref. BENZAC19⁵⁸, where the benzene-like rings stack above the carboxylic acid homosynthon.

There are various reasons for weakly-binding benzene-like motifs, including weak stacking and steric hindrance. As is evident from Fig. 6(c-d), rings will *resist* crystallization when the interactions of the end groups lead to deformation of the ring geometry. Take for example phenanthrene (CSD Ref. PHENAN14⁵⁹, Fig. 6(c)), a high-pressure polymorph that is unstable at ambient conditions (therefore has an overall positive lattice energy for the DFT reference used). Interestingly, we can pinpoint the localization of this deformation by looking at the atoms with the

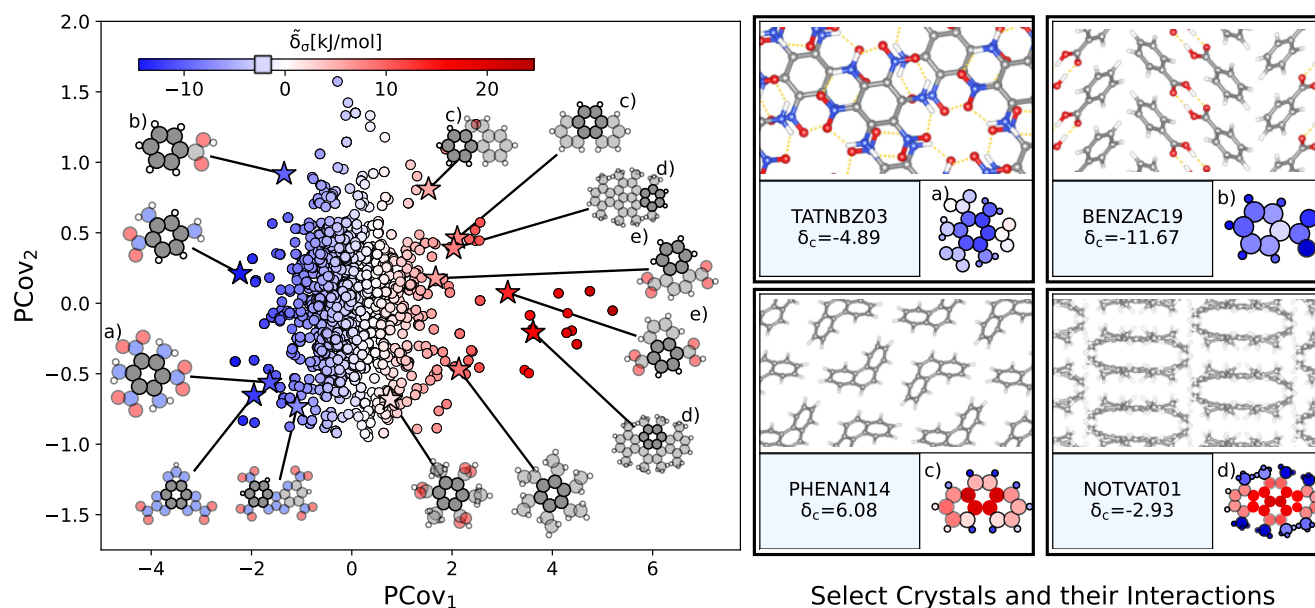


Fig. 6 The Interactions of Benzene-like Rings. (left) Principal Covariates Regression (PCovR) Map, where the color of each point denotes the estimated cohesive interaction of that motif and a marker on the color bar denotes the average value of benzene-like rings. The insets visualize several extremal or interesting motifs. (right) Select crystalline configurations and energy assignments: CSD Refs. (a) TATNBZ03⁵⁷, (b) BENZAC19⁵⁸, (c) PHENAN14⁵⁹, and (d) NOTVAT01⁶⁰. We also highlight the benzene-like motif from Fig. 5(f) in (e). In each panel on the right, the bottom row shows the total lattice energy of the crystal (in kJ/mol) and the corresponding molecules where the atoms have been recolored by their estimated lattice energy contribution (on the same scale as on the left panel).

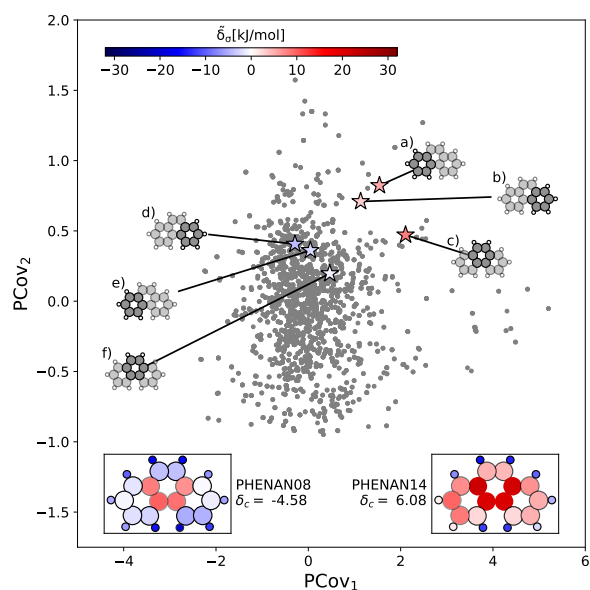


Fig. 7 Comparing the Motifs in Polymorphs of Phenanthrene. Here we project two distinct polymorphs of phenanthrene onto the PCovR map shown in Fig. 6. At ambient conditions, one polymorph is stable (PHENAN08⁶¹), while the other is unstable (PHENAN14⁵⁹, also shown in Fig. 6(c)). Looking at the same motifs in the unstable and stable phases, we see a shift leftwards as the motifs go from resisting crystallization to weakly binding. In the lower insets, we have recolored the atoms of the phenanthrene molecule based upon their contribution to the lattice energy in the different polymorphs. Note that the bicyclic carbon atoms, while no longer distorted, weakly resist crystallization, as they prevent the auxiliary hydrogens from more closely interacting with neighboring π bonds by distorting the molecule.

strongest positive contribution. While the keen reader may infer that this is solely due to the remnant descriptor reflecting the difference in strained and relaxed molecular geometry, we will note that a large difference in these representations can also coincide with a wealth of stabilizing intermolecular interactions, demonstrating that this simple linear model can differentiate molecular deformation from the introduction of new interactions.

This is further supported by comparing the motifs of this unstable polymorph with its stable counterpart (CSD Ref. PHENAN08⁶¹) to see how the nature of the same molecule changes based upon the interactions in the crystal. Both polymorphs adopt a similar herringbone crystal structure; however, the decreased molecular distortion and increased interactions between the auxiliary hydrogens and neighboring aromatic rings in PHENAN08⁶¹ results in a significantly lower lattice energy of $\delta_c = -4.58$. When we project the motifs of PHENAN08⁶¹ and PHENAN14⁵⁹ onto our PCovR map from Fig. 6, we see this reflected by a left-shift of the motifs on the map, where the center ring moves from strongly resisting crystallization (Fig. 7(c)) to weakly interacting (Fig. 7(f)) and the periphery rings move from weakly resisting crystallization (Fig. 7(a,b)) to weakly binding (Fig. 7(e,f)). It is worth noting that PHENAN08⁶¹ is an out-of-sample data point ($\epsilon = 0.2$ kJ/mol), demonstrating that the analysis in Fig. 6 is applicable beyond the fixed reference set. We have included images of the crystal configuration of PHENAN08⁶¹ in the SI.

3.2.4 Nitro Groups

Nitro groups, defined as a nitrogen atom bonded to two terminal oxygen atoms, range in cohesive contributions from -32.7

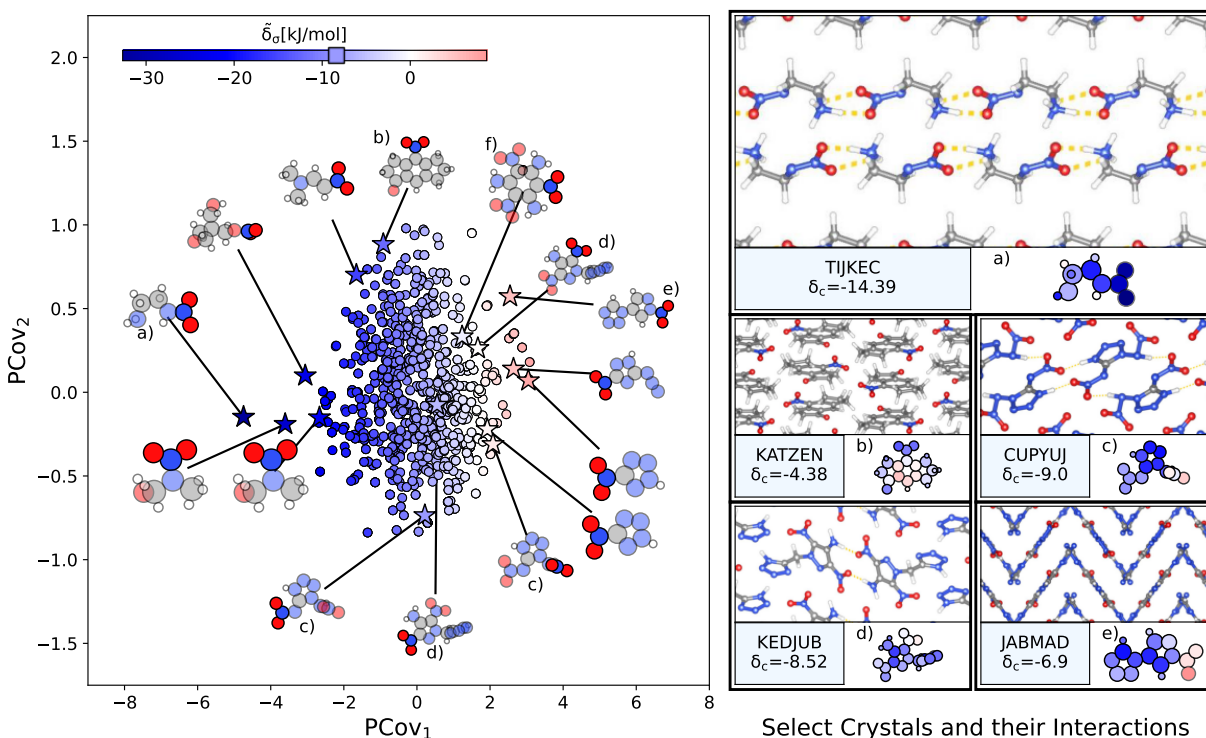


Fig. 8 The Interactions of Nitro Groups. (left) Principal Covariates Regression (PCovR) Map, where the color of each point denotes the estimated cohesive interaction of that motif. (right) Select crystalline configurations and energy assignments: CSD Refs. (a)TIJKEC⁶², (b) CUPYUJ⁶³, (c) KATZEN, (d) KEDJUB⁶⁴, and (e) JABMAD⁶⁵. We also highlight the nitro group of TATNBZ03⁵⁷ from Fig. 6(b) in (f). In each panel on the right, the bottom row shows the total lattice energy of the crystal (in kJ/mol) and the corresponding molecules where the atoms have been recolored by their estimated lattice energy contribution (on the same scale as on the left panel).

kJ/mol to 8.7 kJ/mol, with most interaction strengths being -8.4 ± 5.6 kJ/mol. Similar to our previous examples, we generate a new PCovR using the averaged remnant descriptors and effective interactions of the 2'135 nitro groups, as shown in the left panel of Fig. 8. Again, we have included a panel on the right showing the crystalline conformation and constituent molecules colored by $\tilde{\delta}_a$. Unlike carboxyl and benzene-like groups, the chemical diversity of nitro interactions is limited – this is either due to the chemical nature of nitro interactions or the availability of nitro-containing crystals in CSD.

The resonant or partial charge of the oxygen atoms leads to strong binding in hydrogen-rich environments, supported by the results in Fig. 8. This is best typified by 1-Amino-2-nitraminoethane (CSD Ref. TIJKEC⁶²), a zwitterionic molecule where the nitro group is strongly interacting with the NH_3^+ end group with some potential π -hole stacking⁶⁶ between the N^+-N^- moiety, as shown in Fig. 8(a). The strength of these binding interactions lessens with the strength of the electron donors, with smaller contributions in crystals where the primary $O \cdots H$ interaction is with amine donors (e.g., Fig. 8(d, e), CSD Refs. CUPYUJ⁶³, KEDJUB⁶⁴). In some of these cases, the binding is likely weakened by intramolecular interactions, similar to the contributions of the nitro groups in 2,4,6-trinitrobenzene-1,3,5-triamine (CSD Ref. TATNBZ03⁵⁷, Fig. 8(g), seen earlier in Fig. 6(b)). Finally, to the right of the map, we see the strongest repulsive interactions from nitro groups in proximity to other nitro or aromatic

nitrogen groups, such as the nitro-azole interaction in 1-(1-nitro-1H-pyrazol-4-yl)-1H-tetrazole (CSD Ref. JABMAD⁶⁵, Fig. 8(f)).

4 Conclusions

Molecular crystallization is a complex, multi-faceted process, that poses tremendous challenges to both quantitative modeling, and to the derivation of qualitative design principles. In this work we propose a data-driven strategy to build a database of the interaction motifs that are found in a diverse set of molecular crystals, to determine semi-quantitatively their contribution to the lattice energy, and to generate a library of molecular motifs that can be used to interpret the stability of known crystals and to assist the design of new ones.

In doing so, we have to strike a balance between several conflicting goals. By using a dataset that is constructed by selecting structures from the CSD while maximizing their structural diversity we ensure that we cover a broad range of chemical and packing motifs, while remaining focused on structures that are known to be experimentally realizable. By using a general-purpose, atom-centered structural representation that is capable of describing arbitrary structural correlations we ensure that our data analysis is flexible and that it does not incorporate pre-conceived notions about molecular bonding. At the same time, we ensure that the model focuses on the features that are most relevant to determine crystal stability by building a remnant descriptor that uses isolated molecules as reference – mimicking the

definition of the lattice energy as a difference between the total energies of the crystal and its constituents.

The resulting models achieve a respectable mean absolute error of about 0.4kJ/mol in predicting the atomic contributions to crystal stability using these descriptors, which would not be sufficient to rank different metastable polymorphs of a given compound, but gives us a semi-quantitative estimate of the contribution of each atomic environment to the lattice energy. In order to translate these atomic contributions in a language that can be useful to crystal chemistry, we then assemble them to estimate the stabilizing power of traditional chemical groups (carboxylic acids, amines, ...) and build data-driven maps that facilitate the comparison of different chemical environments, by expressing the greatest amount of structural variability and simultaneously the best correlation with the lattice energy contribution. For each chemical moiety we provide an interactive map (on Materials Cloud⁴⁵) that allows to juxtapose different types of crystal environments, to identify structural patterns that are either stabilizing or destabilizing, and to contrast them with conventional motifs (e.g. hydrogen-bonding), demonstrated here for a few selected cases. With these tools, we aim to enable those designing molecular co-crystals to identify suitable co-formers, reducing the amount of trial-and-error often necessary with crystal synthesis. As we demonstrate for phenanthrene, it is also possible to use these maps to compare polymorphs of the same molecule, and to analyze molecular motifs for a structure that is not part of our original reference set.

We hope that this library of molecular motifs will prove useful to applications to specific crystal-design problems. More in general, we believe that the general ML protocol that we follow, combining regression of the ultimate target property with unsupervised analysis of molecular motifs, can inspire similar applications to the study of other classes of materials, ranging from metal and covalent organic frameworks to self-assembled monolayers and biological systems.

5 Author Contributions

RKC and MC designed the study and wrote the manuscript. RKC computed the molecular energies and geometries, built the machine learning models, and designed the figures. MP separated the crystals into molecular components, screened the dataset before relaxation calculations, started the molecular energy calculations, and edited the manuscript. EAE performed DFT to determine the relaxed crystals and their energies, advised on the dataset provenance and curation, and edited the manuscript.

6 Acknowledgments

This project was funded by NCCR Marvel Inspire Fellowship (MP), NCCR Marvel (RKC, MC), Trinity College (EAE), and ERC Grant 677013-HBMAP (RKC & MC).

The authors would like to acknowledge Federico Giberti, Andrea Anelli, and Guillaume Fraux for fruitful conversations at the study's start and culmination.

Conflicts of interest

There are no conflicts to declare.

Notes and references

- 1 M. A. E. Yousef and V. R. Vangala, *Crystal Growth & Design*, 2019, **19**, 7420–7438.
- 2 M. K. Dudek and K. Druzbecki, *CrystEngComm*, 2022, **24**, 1665–1678.
- 3 L. Iuzzolino, A. M. Reilly, P. McCabe and S. L. Price, *Journal of Chemical Theory and Computation*, 2017, **13**, 5163–5171.
- 4 S. Datta and D. J. W. Grant, *Nature Reviews Drug Discovery*, 2004, **3**, 42–57.
- 5 T. Beyer, G. M. Day and S. L. Price, *Journal of the American Chemical Society*, 2001, **123**, 5086–5094.
- 6 M. M. Azrain, M. R. Mansor, S. H. S. M. Fadzullah, G. Omar, D. Sivakumar, L. M. Lim and M. N. A. Nordin, *Synthetic Metals*, 2018, **235**, 160–175.
- 7 J. Mei, N. L. C. Leung, R. T. K. Kwok, J. W. Y. Lam and B. Z. Tang, *Chem. Rev.*, 2015, **115**, 11718–11940.
- 8 E. Krissinel and K. Henrick, *Journal of Molecular Biology*, 2007, **372**, 774–797.
- 9 Q. C. Zhang, D. Petrey, L. Deng, L. Qiang, Y. Shi, C. A. Thu, B. Bisikirska, C. Lefebvre, D. Accili, T. Hunter, T. Maniatis, A. Califano and B. Honig, *Nature*, 2012, **490**, 556+.
- 10 P. Ganguly and G. R. Desiraju, *CrystEngComm*, 2010, **12**, 817–833.
- 11 R. Davey, G. Dent, R. Mughal and S. Parveen, *Crystal Growth & Design*, 2006, **6**, 1788–1796.
- 12 A. Dey, M. T. Kirchner, V. R. Vangala, G. R. Desiraju, R. Mondal and J. A. Howard, *Journal of the American Chemical Society*, 2005, **127**, 10545–10559.
- 13 J. Sarma and G. R. Desiraju, *Crystal Growth & Design*, 2002, **2**, 93–100.
- 14 G. R. Desiraju, *Angew. Chem. Int. Ed.*, 2007, **46**, 8342–8356.
- 15 M. K. Corpinot and D.-K. Bucar, *Crystal Growth & Design*, 2019, **19**, 1426–1453.
- 16 I. J. Bruno, J. C. Cole, P. R. Edgington, M. Kessler, C. F. Macrae, P. McCabe, J. Pearson and R. Taylor, *Acta Cryst. B*, 2002, **58**, 389–397.
- 17 I. J. Bruno, J. C. Cole, M. Kessler, J. Luo, W. S. Motherwell, L. H. Purkis, B. R. Smith, R. Taylor, R. I. Cooper, S. E. Harris and others, *Journal of Chemical Information and Computer Sciences*, 2004, **44**, 2133–2144.
- 18 M. A. Neumann, F. J. Leusen and J. Kendrick, *Angewandte Chemie*, 2008, **120**, 2461–2464.
- 19 J. Hoja, H.-Y. Ko, M. A. Neumann, R. Car, R. A. DiStasio and A. Tkatchenko, *Science Advances*, 2019, **5**, eaau3338.
- 20 M. A. Spackman and D. Jayatilaka, *CrystEngComm*, 2009, **11**, 19–32.
- 21 M. A. Spackman and J. J. McKinnon, *CrystEngComm*, 2002, **4**, 378–392.
- 22 O. Egorova, R. Hafizi, D. C. Woods and G. M. Day, *The Journal of Physical Chemistry A*, 2020, **124**, 8065–8078.
- 23 F. Musil, S. De, J. Yang, J. E. Campbell, G. M. Day and M. Ce-riotti, *Chem. Sci.*, 2018, **9**, 1289–1300.
- 24 S. Wengert, G. Csányi, K. Reuter and J. T. Margraf, *J. Chem.*

- Theory Comput.*, 2022, **18**, 4586–4593.
- 25 S. Wengert, G. Csányi, K. Reuter and J. T. Margraf, *Chem. Sci.*, 2021, **12**, 4536–4546.
- 26 V. Kapil and E. A. Engel, *Proceedings of the National Academy of Sciences*, 2022, **119**, e2111769119.
- 27 A. Seko, H. Hayashi, K. Nakayama, A. Takahashi and I. Tanaka, *Physical Review B*, 2017, **95**, 144110.
- 28 T. Bereau, D. Andrienko and O. A. von Lilienfeld, *Journal of Chemical Theory and Computation*, 2015, **11**, 3225–3233.
- 29 M. Cordova, E. Engel, A. Stefaniuk, F. Paruzzo, A. Hofstetter, M. Ceriotti and L. Emsley, *Zenodo*, 2022.
- 30 L. Talirz, S. Kumbhar, E. Passaro, A. V. Yakutovich, V. Granata, F. Gargiulo, M. Borelli, M. Uhrin, S. P. Huber, S. Zoupanos, C. S. Adorf, C. W. Andersen, O. Schütt, C. A. Pignedoli, D. Passerone, J. VandeVondele, T. C. Schulthess, B. Smit, G. Pizzi and N. Marzari, *Scientific Data*, 2020, **7**,.
- 31 K. Britts and I. L. Karle, *Acta Cryst.*, 1967, **22**, 308–312.
- 32 M. J. Willatt, F. Musil and M. Ceriotti, *The Journal of Chemical Physics*, 2019, **150**, 154110.
- 33 F. Musil, M. Veit, A. Goscinski, G. Fraux, M. J. Willatt, M. Stricker, T. Junge and M. Ceriotti, *The Journal of Chemical Physics*, 2021, **154**, 114109.
- 34 F. Pedregosa, G. Varoquaux, A. Gramfort, V. Michel, B. Thirion, O. Grisel, M. Blondel, P. Prettenhofer, R. Weiss, V. Dubourg, J. Vanderplas, A. Passos, D. Cournapeau, M. Brucher, M. Perrot and E. Duchesnay, *Journal of Machine Learning Research*, 2011, **12**, 2825–2830.
- 35 B. A. Helfrecht, R. Semino, G. Pireddu, S. M. Auerbach and M. Ceriotti, *The Journal of Chemical Physics*, 2019, **151**, 154112.
- 36 C. Ben Mahmoud, A. Anelli, G. Csányi and M. Ceriotti, *Physical Review B*, 2020, **102**, 235130.
- 37 *SMARTS: A Language for Describing Molecular Patterns*, 1997, daylight.com/dayhtml/doc/theory/theory.smarts.html.
- 38 *RDKit: Open-source cheminformatics.*, <https://www.rdkit.org>.
- 39 S. De Jong and H. A. Kiers, *Chemometrics and Intelligent Lab. Sys.*, 1992, **14**, 155–164.
- 40 B. A. Helfrecht, R. K. Cersonsky, G. Fraux and M. Ceriotti, *Machine Learning: Science and Technology*, 2020, **1**, 045021.
- 41 S. Janeda and D. Mootz, *Zeitschrift für Naturforschung B*, 1999, **54**, 103–108.
- 42 R. D. L. Johnstone, A. R. Lennie, S. Parsons, E. Pidcock and J. E. Warren, *Acta Crystallographica Section B*, 2009, **65**, 731–748.
- 43 M. Schreyer, L. Guo, S. Thirunahari, F. Gao and M. Garland, *Journal of Applied Crystallography*, 2014, **47**, 659–667.
- 44 T. M. Klapötke, M. Q. Kurz, R. Scharf, P. C. Schmid, J. Stierstorfer and M. Sućeska, *ChemPlusChem*, 2015, **80**, 97–106.
- 45 R. K. Cersonsky, M. Pakhnova, E. A. Engel and M. Ceriotti, *Lattice Energies for a Diverse Set of Molecular Crystals*, 2022.
- 46 A. Briceño, D. Leal, G. Ortega, G. D. d. Delgado, E. Ocando and L. Cubillan, *CrystEngComm*, 2013, **15**, 2795–2799.
- 47 A. Cruz-Cabeza, G. Day and W. Jones, *Chemistry – A European Journal*, 2008, **14**, 8830–8836.
- 48 P. Roussel, F. Bentiss, M. Drache, P. Conflant, M. Lagrenee and J.-P. Wignacourt, *Journal of Molecular Structure*, 2006, **798**, 134–140.
- 49 J. Derissen, D. JL, S. JC and others, *Crystal Structure Communications*, 1979, **8**, 533.
- 50 T. K. Chen, D. C. Ales, N. C. Baenziger and D. F. Wiemer, *The Journal of Organic Chemistry*, 1983, **48**, 3525–3531.
- 51 M. C. Etter, *Accounts of Chemical Research*, 1990, **23**, 120–126.
- 52 M. C. Etter, *The Journal of Physical Chemistry*, 1991, **95**, 4601–4610.
- 53 P. Vishweshwar, A. Nangia and V. M. Lynch, *The Journal of Organic Chemistry*, 2002, **67**, 556–565.
- 54 T. R. Shattock, K. K. Arora, P. Vishweshwar and M. J. Zaworotko, *Crystal Growth & Design*, 2008, **8**, 4533–4545.
- 55 P. Chen, Z. Zhang, S. Parkin, P. Zhou, K. Cheng, C. Li, F. Yu and S. Long, *Royal Society of Chemistry Advances*, 2016, **6**, 81101–81109.
- 56 L. Leiserowitz, *Acta Cryst. B*, 1976, **32**, 775–802.
- 57 Z. Chua, C. G. Gianopoulos, B. Zarychta, E. A. Zhurova, V. V. Zhurov and A. A. Pinkerton, *Crystal Growth & Design*, 2017, **17**, 5200–5207.
- 58 W. Cai and A. Katrusiak, *CrystEngComm*, 2012, **14**, 4420.
- 59 F. P. A. Fabbiani, D. R. Allan, W. I. F. David, S. A. Moggach, S. Parsons and C. R. Pulham, *CrystEngComm*, 2004, **6**, 505–511.
- 60 A. Sygula, F. R. Fronczek and P. W. Rabideau, *Tetrahedron Letters*, 1997, **38**, 5095–5098.
- 61 V. Petříček, I. Císařová, L. Hummel, J. Kroupa and B. Březina, *Acta Crystallographica Section B*, 1990, **46**, 830–832.
- 62 A. Sygula, F. R. Fronczek and P. W. Rabideau, *Tetrahedron Letters*, 1997, **38**, 5095–5098.
- 63 D. Fischer, T. M. Klapötke and J. Stierstorfer, *Angewandte Chemie International Edition*, 2015, **54**, 10299–10302.
- 64 D. Kumar, G. H. Imler, D. A. Parrish and J. M. Shreeve, *Chemistry*, 2017, **23**, 7876–7881.
- 65 I. A. Vatsadze, O. V. Serushkina, M. D. Dutov, T. K. Shkineva, K. Y. Suponitsky, B. I. Ugrak and I. L. Dalinger, *Chemistry of Heterocyclic Compounds*, 2015, **51**, 695–703.
- 66 A. Bauzá, T. J. Mooibroek and A. Frontera, *Chem. Comm.*, 2015, **51**, 1491–1493.
- 67 C. S. Adorf, V. Ramasubramani, B. D. Dice, M. M. Henry, P. M. Dodd and S. C. Glotzer, *glotzerlab/signac*, 2019, <https://doi.org/10.5281/zenodo.2581326>.
- 68 C. S. Adorf, P. M. Dodd, V. Ramasubramani and S. C. Glotzer, *Computational Materials Science*, 2018, **146**, 220–229.
- 69 B. Hourahine, B. Aradi, V. Blum, F. Bonafé, A. Buccheri, C. Camacho, C. Cevallos, M. Y. Deshayé, T. Dumitrică, A. Dominguez, S. Ehlert, M. Elstner, T. van der Heide, J. Hermann, S. Irle, J. J. Kranz, C. Köhler, T. Kowalczyk, T. Kubař, I. S. Lee, V. Lutsker, R. J. Maurer, S. K. Min, I. Mitchell, C. Negre, T. A. Niehaus, A. M. N. Niklasson, A. J. Page, A. Pecchia, G. Penazzi, M. P. Persson, J. Řezáč, C. G. Sánchez, M. Sternberg, M. Stöhr, F. Stuckenberg, A. Tkatchenko, V. W.-z. Yu

- and T. Frauenheim, *The Journal of Chemical Physics*, 2020, **152**, 124101.
- 70 M. Gaus, A. Goez and M. Elstner, *Journal of Chemical Theory and Computation*, 2013, **9**, 338–354.
- 71 M. Gaus, X. Lu, M. Elstner and Q. Cui, *Journal of Chemical Theory and Computation*, 2014, **10**, 1518–1537.
- 72 P. Giannozzi, S. Baroni, N. Bonini, M. Calandra, R. Car, C. Cavazzoni, D. Ceresoli, G. L. Chiarotti, M. Cococcioni, I. Dabo, A. Dal Corso, S. de Gironcoli, S. Fabris, G. Fratesi, R. Gebauer, U. Gerstmann, C. Gougoussis, A. Kokalj, M. Lazzeri, L. Martin-Samos, N. Marzari, F. Mauri, R. Mazzarello, S. Paolini, A. Pasquarello, L. Paulatto, C. Sbraccia, S. Scandolo, G. Sclauzero, A. P. Seitsonen, A. Smogunov, P. Umari and R. M. Wentzcovitch, *Journal of Physics: Condensed Matter*, 2009, **21**, 395502.
- 73 J. Perdew, K. Burke and M. Ernzerhof, *Physical Review Letters*, 1996, **77**, 3865–3868.
- 74 S. Grimme, *Journal of Computational Chemistry*, 2006, **27**, 1787–1799.
- 75 A. Dal Corso, *Computational Materials Science*, 2014, **95**, 337–350.
- 76 G. Kresse and D. Joubert, *Phys. Rev. B*, 1999, **59**, 1758–1775.
- 77 G. J. Martyna and M. E. Tuckerman, *The Journal of Chemical Physics*, 1999, **110**, 2810–2821.
- 78 M. J. Willatt, F. Musil and M. Ceriotti, *Phys. Chem. Chem. Phys.*, 2018, **20**, 29661–29668.
- 79 N. M. O’Boyle, M. Banck, C. A. James, C. Morley, T. Vandermeersch and G. R. Hutchison, *Journal of Cheminformatics*, 2011, **3**, 33.

A Constructing the Dataset

A.1 Dataset Curation

We start with a dataset containing approximately 10'600 ground-state, geometry-optimized configurations originally used for training (10'000) and testing (604) a model for predicting NMR chemical shieldings for organic molecular crystals²⁹. These molecular crystals contain 14 of the most common chemical species, and their energies have already been computed using the protocol described in Sec. A.2. For our study, we selected all H, C, N, O, and S-containing molecular crystals composed of non-polymeric, neutrally-charged molecules and less than 200 atoms per unit cell. This resulted in 2'823 and 558 such crystals for training and testing, corresponding to 3'242 and 628 molecules, respectively. All data and workflows were managed by the *signac* and *signac-flow* packages^{67,68}.

Reducing to H, C, N, O, S First, we eliminated all structures containing chemical species other than H, C, N, O, and S. We have limited our dataset to these species to maximize the diversity of our dataset while minimizing the size of our SOAP representation (the length scales with $\mathcal{O}(n_{\text{species}}^2)$). This resulted in the largest reduction of the overall dataset, from roughly 10'000 to 3'800 crystals.

Separating the Crystals We then separated each crystal into its molecular constituents. First, we computed radial distribution functions, combining the data from all structures in a single histogram for each pair of chemical species. We determined the cutoff distance for covalent bonds as the first near-zero minimum after the first neighbor peak. We computed a supercell consisting of $3^3 \cdot 7^3$ repeat unit cells for each crystal to screen for polymers, where we eliminated non-terminating molecules (*e.g.*, those that continued to increase in size with each supercell addition).

Determining the Set of Unique Molecules Finally, we determined the irreducible set of constituent molecules by identifying identical/redundant molecules based on the similarity of their SOAP features. In practice, a similarity kernel $K_{mm'} = \mathbf{x}_m \cdot \mathbf{x}_{m'}$ was constructed by computing the similarity of each pair of molecules m and m' and iteratively removing molecules $m' > m$, for which $K_{mm'} > \epsilon$. For the later step of identifying the molecular motifs, we were careful to index the location of each atom in the original crystal within the constituent molecules. Furthermore, we compute the binding energy based on the lowest energy conformer represented in the dataset, ensuring comparability between crystals and co-crystals of similar stoichiometries without needing to obtain the global minimum conformation of each molecule (instead relaxing to the local minimum, as discussed in A.2).

Eliminating Charged Molecules We computed the molecular charges from density-functional tight-binding (DFTB) calculations, using the DFTB+ package⁶⁹ and the Third-Order Parameterization for Organic and Biological Systems (3OB)^{70,71} to perform a Γ -point calculation for each crystal structure. Structures containing molecules carrying an absolute charge greater than 0.5e were eliminated. This ensures that *for the given dataset* the lattice energies are defined unequivocally.

A.2 Relaxing Molecular Geometries

Quantum-Espresso Parameterization To ensure that the resultant geometries and energies are consistent and comparable to those obtained for the crystal structures in Cordova *et al.*²⁹, the geometry optimizations for the molecules were performed using the same computational parameters using Quantum Espresso⁷². These parameters were as follows: the PBE exchange-correlation functional⁷³, the D2 dispersion correction⁷⁴, ultrasoft pseudopotentials with GIPAW reconstruction^{75,76}, and an equivalent plane-wave energy cutoff of 60 Ryd. We converged the energies within 1E-4 Ryd and forces below 1E-3 Ryd/Bohr, respectively.

Simulation Boxes for Molecules *in vacuo* To determine the simulation boxes appropriate to describe the molecules *in vacuo*, we performed Γ -point calculations. We converged the results with respect to the size of the simulation cell and, *e.g.*, the separation between the periodic images of the molecules. Based on calculations using a variety of simulation cell sizes for 20 different molecules, we determined a minimum vacuum padding of 2-4 times the largest dimension of the molecule proved sufficient to converge the resultant molecular energies. We confirmed these results against those obtained using Martyna-Tuckerman electrostatic decoupling⁷⁷.

B Methods

B.1 SOAP Hyperparameters

SOAP descriptors were generated using the Librascal library³³ (commit 6f7a4002) using the following hyperparameters:

- max_radial: 8
- max_angular: 4
- interaction_cutoff: 7.0
- gaussian_sigma_constant: 0.3
- cutoff_smooth_width: 0.5
- soap_type: "PowerSpectrum"
- gaussian_sigma_type: "Constant"
- radial_basis: "GTO"
- cutoff_function_type: "RadialScaling"
- cutoff_function_parameters: {rate: 1.5, exponent: 3.0, scale: 2.0}

As tuning these hypers could favor one representation over another, we chose cutoff and scaling parameters to be consistent with the chemical geometry, noting that changing these parameters within this range has minimal effect on the errors. We determined the number of radial and angular channels (corresponding to the "resolution" of the descriptors) by balancing the number of features in each feature vector with the in-sample error of δ . The resulting SOAP vectors included 3-body correlations for each atomic neighborhood up to 7Å, weighting neighbor contributions with a radial scaling procedure introduced in Willatt *et al.*⁷⁸.

B.2 Filtering the Environmental Contributions

As noted in the main text, we applied a filtering scheme to the estimated contributions of each atomic environment. This technique reduces the number of extreme contributions attributed to any given environment, as shown in the changes in distribution in Fig. S1.

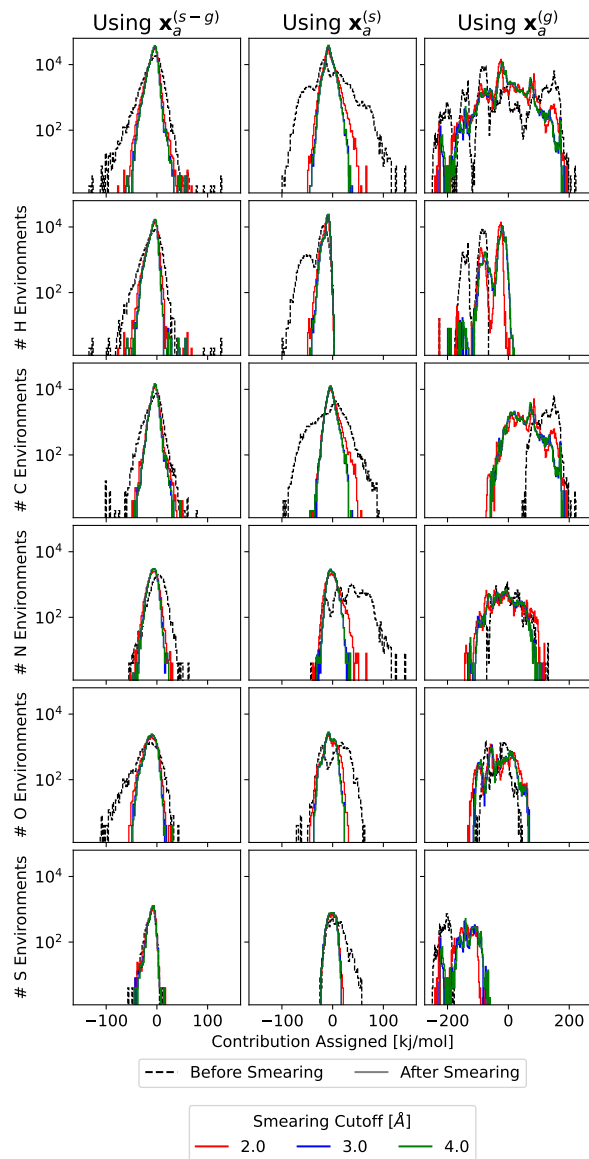


Fig. S1 Effect of “Smearing” the Contributions using Eq. (9).

Notice that all of these vary based on representation and environment. In most cases, we see the distribution narrow with the smearing – signifying a regularization to the estimated contributions (*e.g.*, dampening of extreme values). The smearing converges to a constant set of contributions with an increasing smearing cutoff, typically 2.0-3.0 Å (we use 2.0Å for all results in the text).

B.3 Identifying Molecular Motifs

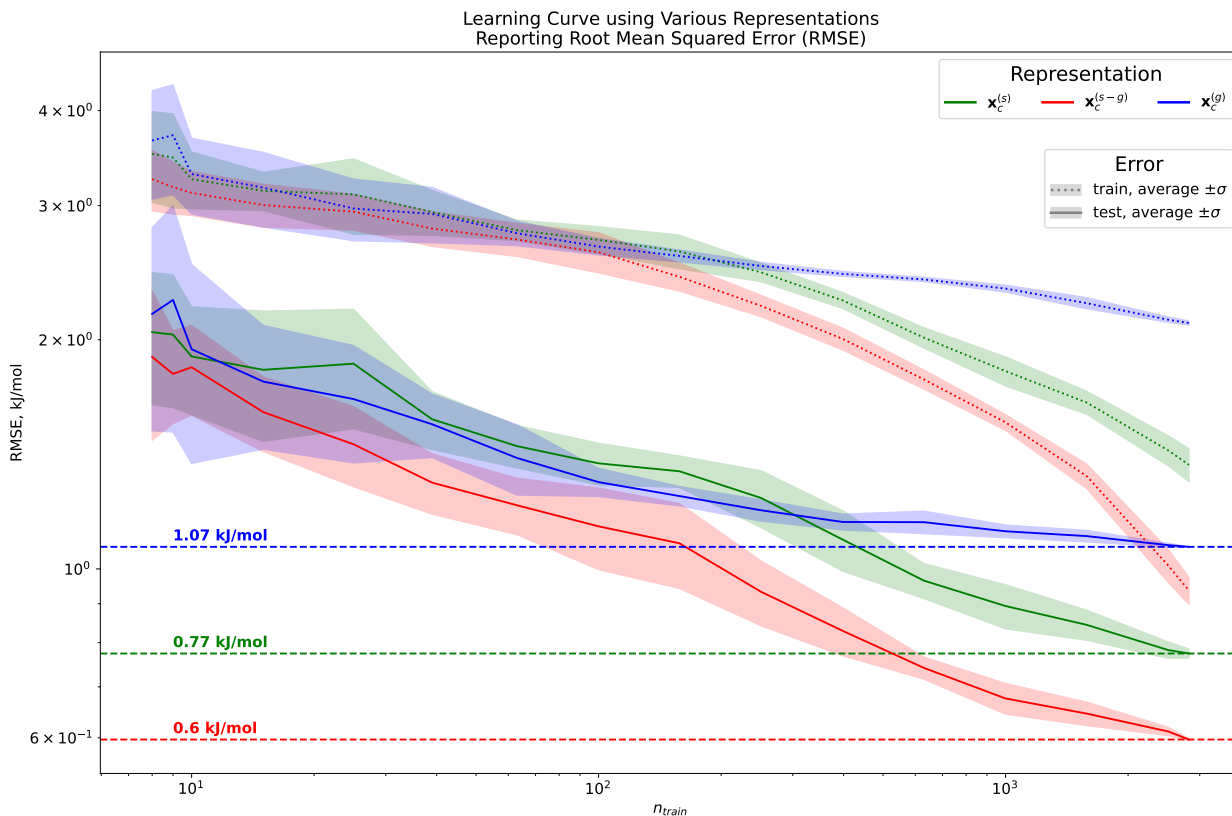
We employed RDKit Substructure Matching³⁸ to identify the molecular motifs. For this, we took (our typical) .xyz format of the molecular geometries and converted them to .mol format using the openbabel software⁷⁹. We label the functional groups for zwitterionic molecules based on their configuration in the crystal. Zwitterionic molecules were prone to redistribute charges upon relaxation, which led to a change in configurational connectivity and misclassification. This affected roughly 600 of the 70'000 molecular motifs – all other molecules retained the same connectivity upon relaxation. When labeling each collection of atoms, we assign each fragment its most specific designation, *e.g.*, each *nitro* group was not also considered as two *nitroso* groups. We used the SMARTS strings³⁷ listed in Table S1 to identify motifs in the molecules.

	Name	SMARTS String	# Instances
Sulfur-Based	Aromatic Sulfurs	s	1393
	Disulfide	[#6]~[#16;X2]~[#16;X2]~[#6]	290
	Sulfide Chain	[#16]~[#16;X2]~[#16;X2]~[#16]	200
	Sulfinamide	[SX3] (~[OX1]) (~[#6])~[#7]	7
	Sulfinyl	[!#8]~[#16;X3] (~[!#8])~[OX1]	194
	Sulfonate Esters	[SX4] (~[OX1]) (~[OX1]) ([#6])~[O;X2,-]	136
	Sulfonyl	[!#8]~[#16;X4] (~[OX1]) (~[!#8])~[OX1]	549
	Thiocarbonyl	C~[SX1]	375
	Thiocarboxamide	[#1,#6]~C(~[SX1])[#7]	176
	Thioether	[#6]~[SX2]~[#6]	2062
	Thioketone	[#6]~[#6] (~[S;X1])[#6]	44
	Thiol	[#6;!\$(C=,#[!#6])] [SX2H]	58
	Thiourea	[#7]~C(~[SX1])[#7]	318
Nitrogen-Based	Aromatic Nitrogens	n	9268
	Aryl Amines	[N\$(N-c);H1,H2;r0]	1171
	3° Amines	[#7;X3;H0] ([#6]) ([#6]) [#6]	1911
	2° Amines	[#7;X3;H1] ([#6]) [#6]	2559
	1° Amines	[#7;X3;H2] [#6]	782
	Acetamide	[#7;X3]~[#6;X3]~[O;X1]	3593
	Azide	[#7;X2]~[#7;X2]~[#7;X1]	266
	Azo	[#6]-N=N-[#6]	115
	Carbamide	[#7;X3]~C(~[O;X1])~[#7;X3]	405
	Hydrazine	[#7;X3]~[#7;X3;H2]	414
	Hydroxylamines	[#6]~[#7;X3] (~[#6])~[#8;H1]	92
	Nitrile	[#6]~[#7;X1]	68
	Nitro	[#8;X1]~[#7]~[#8;X1]	2135
	Nitroso	[#7]~[#8;X1]	506
	Oxime	[#6]~[#7;X2]~[#8;H1]	299
NH ₃ ⁺	[#7;X4;H3]	241	
Carbon-Based	Carboxylates	[O;X1]~C~[O;-]	334
	Carboxyls	[O;X1]~C~[O;H1]	1109
	Carbonyls	[#6,#7,#1]~[C!\$(C;X3] (~[#8])~[#8]) (~[#6,#8,#1])~[O;X1]	102
	Alcohols	[#6!\$(#6=O)]~[O;H1]	2691
	Carbonate	[#8;X2]~[C] (~[#8;X1])~[#8;X2]	54
	Epoxide	O1CC1	252
	Ester	C(~[O;X1])~[O;H0;X2]~C	1228
	Ether	[#8;X2] (~C)~C	1776
	Ketone	[#6] [CX3] (~[O;X1]) [#6]	1041
	Peroxides	[#8;X2]~[O;X2]	95
	Water	[OH2]	1030
Carbon-Based	Aromatic Carbons	[c]	12161
	Alkane	[C;H2,H3]~[C;H2,H3]	5721
	Alkene	[C;H1,H0]=[C;H1,H0]	2471
	Alkyne	[C]#[C;H1]	8
	Benzene-like Rings	c1ccccc1	3348
	Methyl	[C;H3;X4]	5777
	Methylene Bridges	[C;X4;H2;r0]	541
	Vinyl	[C;H2;X3]	233

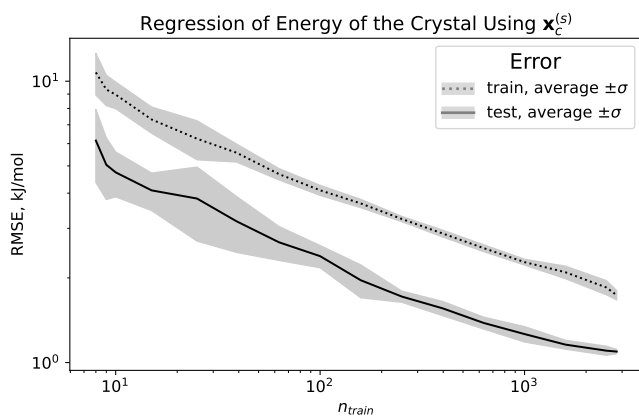
Table S1 Table of SMARTS Strings used to Identify Molecular Motifs. Notice that some SMARTS strings deviate from typical convention in order to accommodate the translation from thermodynamic coordinates (.xyz) to molecular connectivity graph format (.mol), as well as to define certain groups as mutually exclusive.

C Additional Results and Visualizations

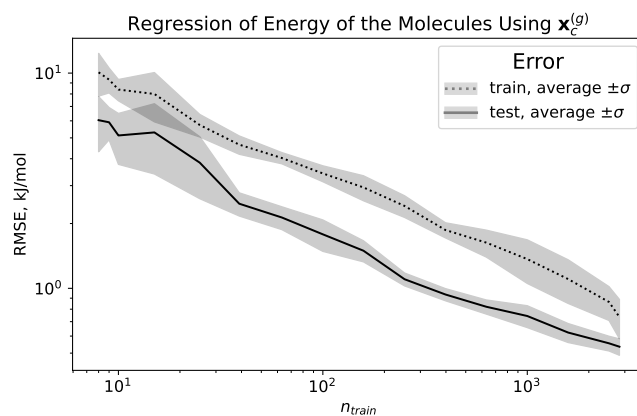
C.1 Learning Curves



(a) Learning Curve of Various Representations on δ .



(b) Learning Curve of $\mathbf{x}_c^{(s)}$ on e_c .



(c) Learning Curve of $\mathbf{x}_c^{(g)}$ on e_m .

Fig. S2 Learning curves for lattice energy for the various representations used in this study. We varied the ratio of mutually-exclusive and randomly-selected training and testing points in each learning curve and conducted a 5-fold cross-validated ridge regression. For each ratio, we conducted ten trials with random training sets and report the average (line) and standard deviations (shaded area).

For each descriptor, we constructed learning curves to demonstrate the saturation (or lack thereof) of the regression model on lattice energy. Each learning curve was run using `scikit-learn.model_selection.learning_curve` using a 10-fold cross-validation on a 5-fold cross-validated ridge regression pulling randomly from our established training set. All learning curves demonstrate that we are still within a small-data regime (noted by the absence of saturation), justifying our focus on simple and data-efficient linear models.

C.2 Kernel Ridge Regression Models

Kernel Type	Structure-Wise Definition $K_{AB} = \frac{1}{n_A n_B} \sum_{a,b} \dots$	Equivalent RKHS Definition $K =$
Crystal Environments	$k(\mathbf{x}_a^{(s)}, \mathbf{x}_b^{(s)})$	$\phi_c^{(s)} (\phi_{c'}^{(s)})^T$
Molecular Environments	$k(\mathbf{x}_a^{(g)}, \mathbf{x}_b^{(g)})$	$\phi_c^{(g)} (\phi_{c'}^{(g)})^T$
Remnant of the RKHS Features	$k(\mathbf{x}_a^{(s)}, \mathbf{x}_b^{(s)}) + k(\mathbf{x}_a^{(g)}, \mathbf{x}_b^{(g)})$ $- k(\mathbf{x}_a^{(s)}, \mathbf{x}_b^{(g)}) - k(\mathbf{x}_a^{(g)}, \mathbf{x}_b^{(s)})$	$\left[(\phi_c^{(s)} - \phi_c^{(g)}) (\phi_{c'}^{(s)} - \phi_{c'}^{(g)})^T \right]$
Remnant Environments	$k(\mathbf{x}_a^{(s-g)}, \mathbf{x}_b^{(s-g)})$	$\phi_c^{(s-g)} (\phi_{c'}^{(s-g)})^T$

Table S2 Equations for Non-linear Kernels We computed regressions using the given kernel equations for crystals A and B and their corresponding atoms a and b . Mercer’s theorem ensures that for a positive-definite kernel on x , there exists a non-linear mapping $x \mapsto \phi$ such that $K = \phi\phi^T$, for which we have included our notation.

We computed regressions with both (i) an optimized RBF kernel (with optimal γ found by employing a subset of 1,000 crystals taken from the training set and (ii) a parameter-free cosine kernel. We ran kernel ridge regression models using `scikit-learn.linear_model.KernelRidge`³⁴ employing a 90/10 training / validation split. The results on the offset test set are given in Table S3.

Regression Equation	RBF Kernel		Cosine Kernel	
	RMSE	MAE	RMSE	MAE
$\mathbf{e}_c = \left[\phi_c^{(s)} (\phi_{c'}^{(s)})^T \right] \mathbf{w}_c$	0.87	0.656	0.99	0.758
$\mathbf{e}_m = \left[\phi_m^{(g)} (\phi_{m'}^{(g)})^T \right] \mathbf{w}_m$	0.38	0.304	0.473	0.374
$\delta_c = \left[\phi_c^{(s)} (\phi_{c'}^{(s)})^T \right] \mathbf{w}_c$ $- \sum_{m \in c} \frac{n_m}{n_c} \left(\left[\phi_m^{(g)} (\phi_{m'}^{(g)})^T \right] \mathbf{w}_m \right)$	0.86	0.647	0.992	0.757
$\delta_c = \left[\phi_c^{(s)} (\phi_{c'}^{(s)})^T \right] \mathbf{w}$	0.705	0.512	0.744	0.551
$\delta_c = \left[\phi_c^{(g)} (\phi_{c'}^{(g)})^T \right] \mathbf{w}$	1.093	0.72	1.101	0.726
$\delta_c = \left[(\phi_c^{(s)} - \phi_c^{(g)}) (\phi_{c'}^{(s)} - \phi_{c'}^{(g)})^T \right] \mathbf{w}$	0.546	0.404	0.59	0.434
$\delta_c = \left[\phi_c^{(s-g)} (\phi_{c'}^{(s-g)})^T \right] \mathbf{w}$	0.602	0.445	0.656	0.483

Table S3 Results of Kernel Ridge Regression Exercises. We have written each equation using reproducing kernel hilbert space (RKHS) notation (see Table S2), denoting the training set with $'$. Note the difference between the bottom entries, which represent (1) the “remnant version of non-linear feature vectors ϕ and (2) the non-linear mapping of the remnant vector employed in the main text. In each kernel regression, an independent, 2-fold cross-validated model was built on our 2’823 crystal training set in an 80/20 train/validation split. Here we report the RMSE and MAE (in kJ/mol) on a separate testing set of 558 crystals (or the coinciding 628 molecules). Each regression equation \mathbf{w} is unique to that regression.

C.3 Expanded Violin Plot

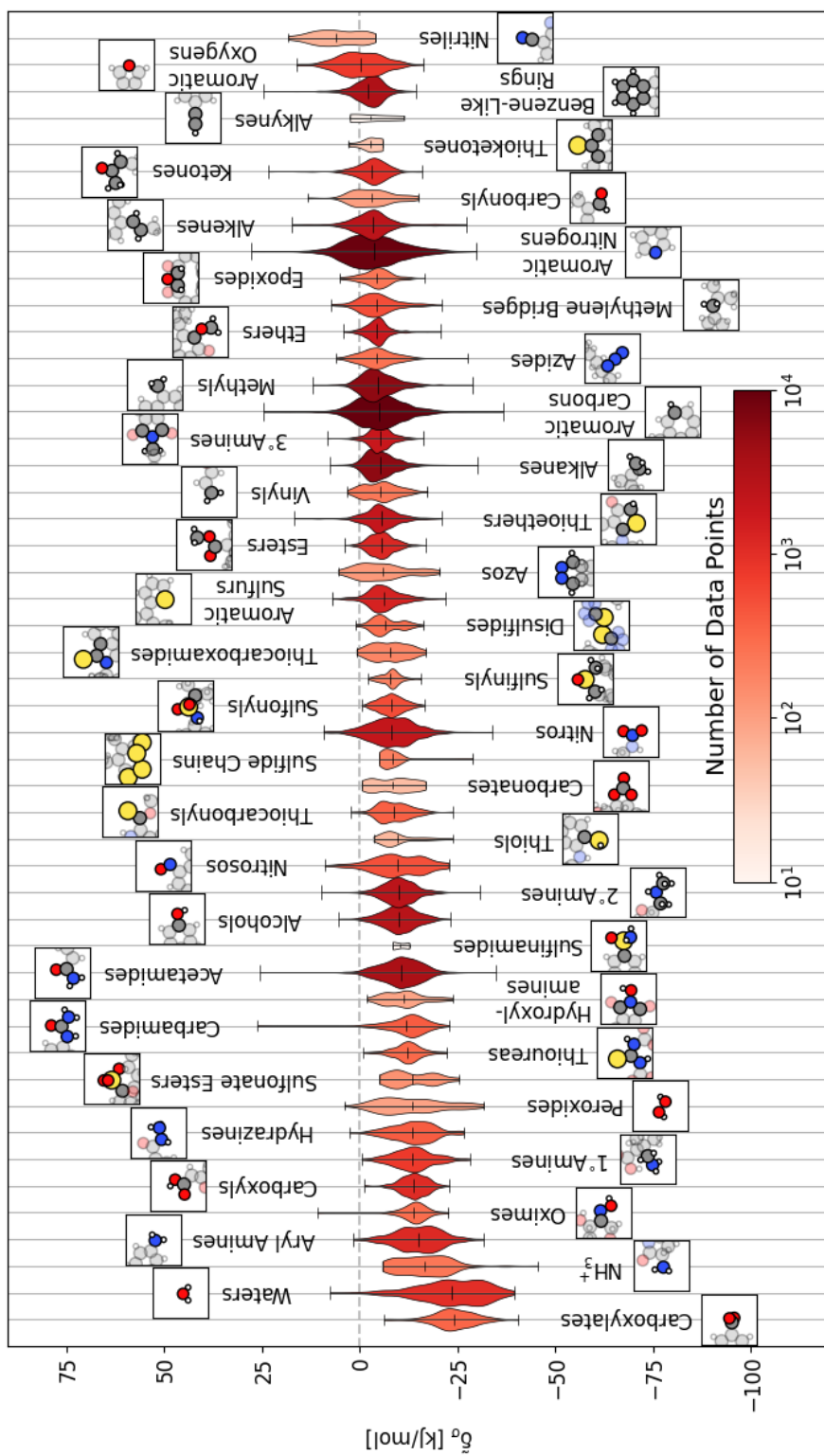
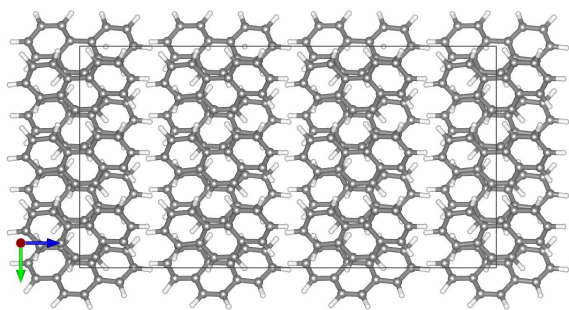
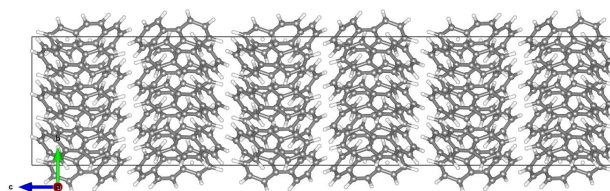


Fig. S3 Violin Plot from Fig. 2, expanded to include all functional groups. A representative example is shown above or below the violin plot with the functional group highlighted for each functional group. The lines on each plot denote each group's extrema and mean contributions. The plots colors reflect the number of examples within the dataset, ranging from 7 (Sulfonamide) to 12'161 (Aromatic Carbon).

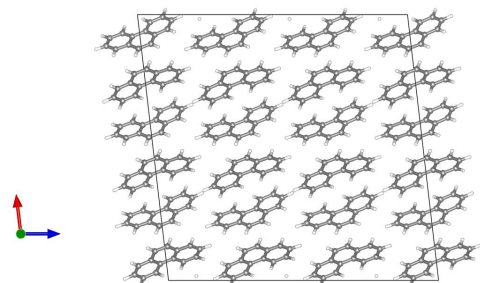
C.4 Images of Phenanthrene Polymorphs



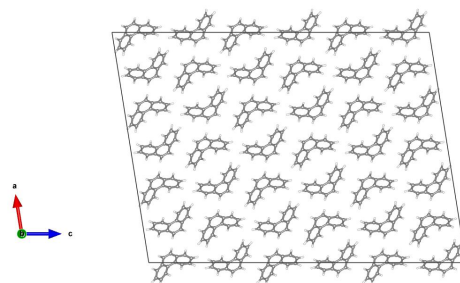
(a) View of PHENAN08⁶¹ along *a* axis.



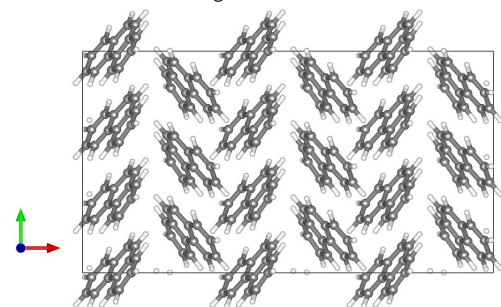
(b) View of PHENAN14⁵⁹ along *a* axis.



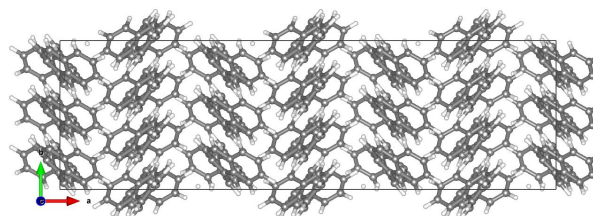
(c) View of PHENAN08⁶¹ along *b* axis.



(d) View of PHENAN14⁵⁹ along *b* axis.



(e) View of PHENAN08⁶¹ along *c* axis.



(f) View of PHENAN14⁵⁹ along *c* axis.

Fig. S4 Axial views of the stable (a, c, e) and unstable (b, d, f) phenanthrene polymorphs. 3x3x3 supercells are shown to include all intermolecular interactions.

C.5 Additional PCovR Maps

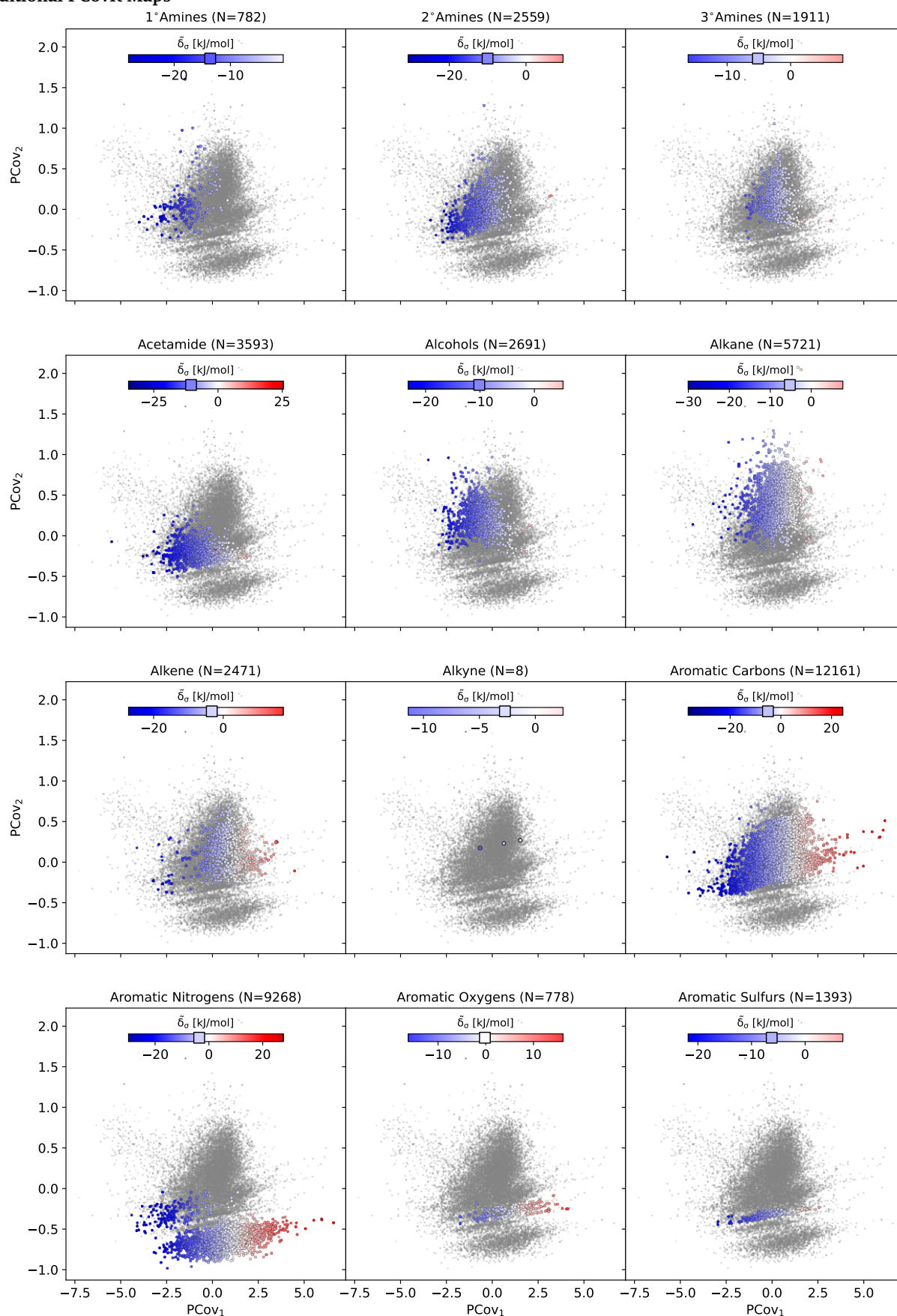


Fig. S5 PCovR map from Fig. 3, highlighting each type of functional group. Each map is on the same color scale; however, we have truncated the color bar to demonstrate the range of cohesive interactions. We have denoted the average of all group members by a square marker on the color bar.

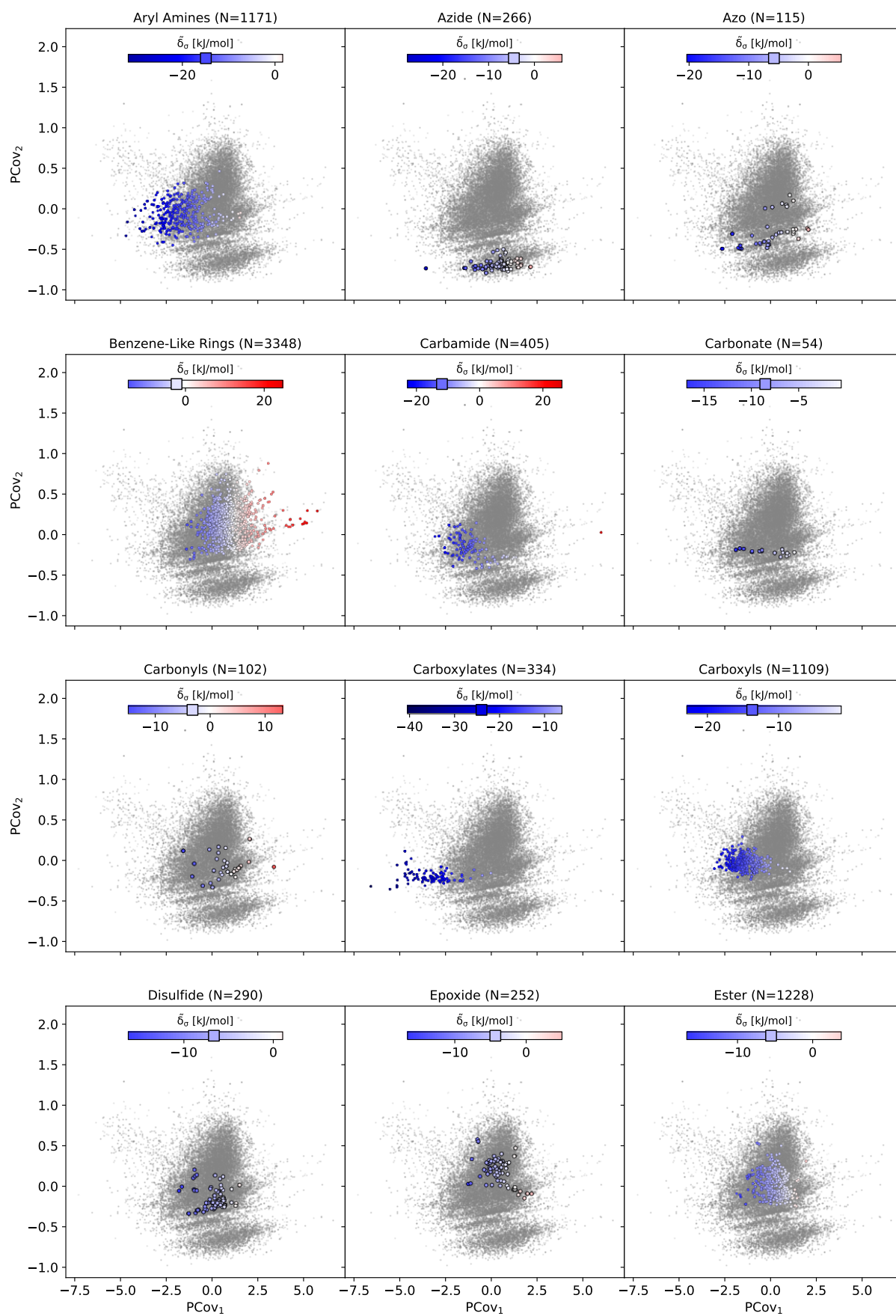


Fig. S6 PCovR map from Fig. 3, highlighting each type of functional group. Each map is on the same color scale; however, we have truncated the color bar to demonstrate the range of cohesive interactions. We have denoted the average of all group members by a square marker on the color bar.

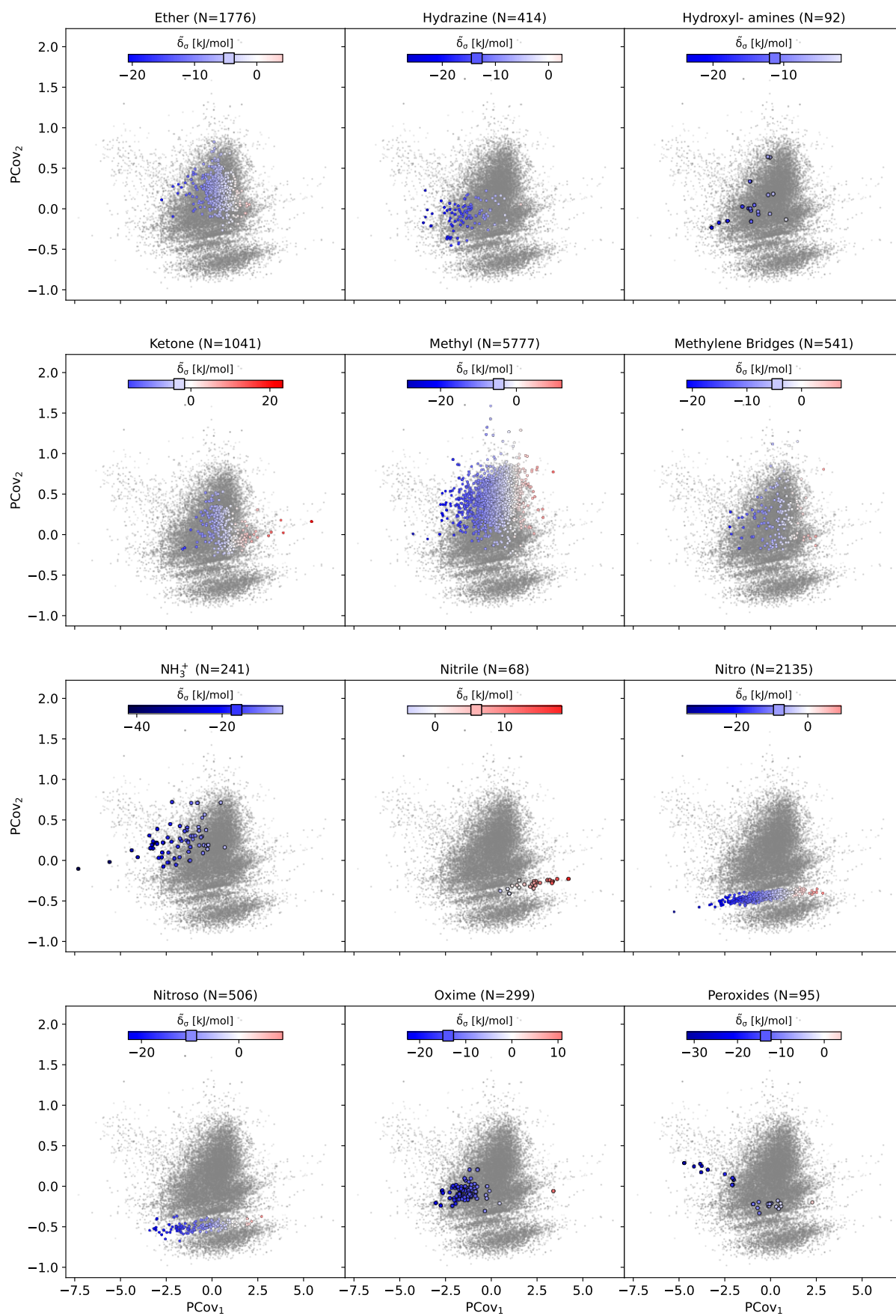


Fig. S7 PCovR map from Fig. 3, highlighting each type of functional group. Each map is on the same color scale; however, we have truncated the color bar to demonstrate the range of cohesive interactions. We have denoted the average of all group members by a square marker on the color bar.

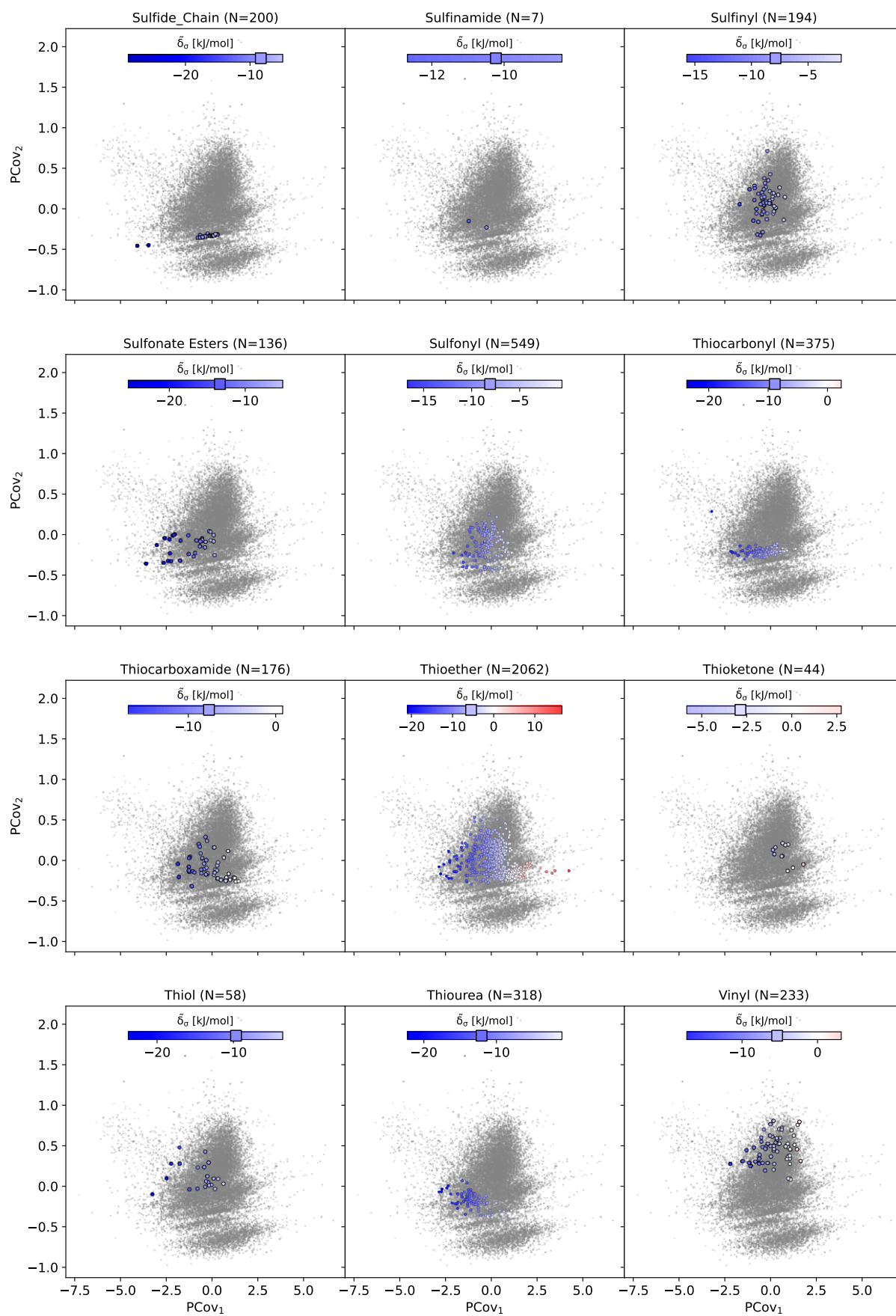


Fig. S8 PCovR map from Fig. 3, highlighting each type of functional group. Each map is on the same color scale; however, we have truncated the color bar to demonstrate the range of cohesive interactions. We have denoted the average of all group members by a square marker on the color bar.